

Revisiting a local, real-space approach to dielectric screening calculations

John Vinson^{1,*} and Eric L. Shirley²

¹*Material Measurement Laboratory, National Institute of Standards and Technology, Gaithersburg, MD 20899*

²*Physical Measurement Laboratory, National Institute of Standards and Technology, Gaithersburg, MD 20899*

(Dated: May 19, 2020)

Various many-body perturbation theory techniques for calculating electron behavior rely on W , the screened Coulomb interaction. The screening requires complete knowledge of the dielectric response of the electronic system, and the fidelity of the calculated dielectric response limits the reliability of predicted electronic and structural properties. As a simplification, calculations often begin with the random phase approximation (RPA). However, even RPA calculations are costly and scale poorly, typically as N^4 (N representing the system size). A local approach has been shown to be efficient while maintaining accuracy [Ultramicroscopy **106**, 986 (2006)]. We present improvements to the accuracy and execution of this scheme, including reconstruction of the all-electron character of the pseudopotential-based wave functions, improved $N^2 \log N$ scaling, and a parallelized implementation. We discuss applications to Bethe-Salpeter equation (BSE) calculations of core and valence spectroscopies.

I. INTRODUCTION

For condensed matter systems, one of the fundamental properties is the dielectric response. This is closely related to the polarizability, the movement of the constituent, electrically charged, electrons and ions that is responsible for any difference between the applied and total potentials. Here we limit our investigation to the electronic behavior of the system, treating the ions as stationary. The dielectric response determines conductivity as well as frequency-dependent absorption and transmission of photons. The polarizability is used in many-body perturbation theory to more accurately determine electronic properties. In calculations of a variety of properties of condensed matter systems, band alignment, optical absorption, adsorption energies, etc., the determination of the electronic response plays a vital role.

Calculations of electron polarizability in condensed systems are commonplace. For a periodic system (infinite crystal), the polarizability is typically calculated in reciprocal space based on the spectral representation of the Green's function or a sum over states [2]. More recently, real-space approaches have also been considered [3–5]. Alternative methods based on many-body perturbation theory have also been suggested [6, 7]. However, all of these approaches scale with system size N of the order N^4 [8]. Imaginary time techniques have been shown to reduce the scaling to N^3 [9–11]. Here, we focus on a localized, real-space approach originally introduced in Ref. [1]. This approach uses a model dielectric response to capture the behavior of the polarizability at long distances while maintaining the accuracy of the random phase approximation (RPA) or time-dependent density-functional theory (TD-DFT) at short distances. It was shown that this approximation was sufficiently accurate for calculating near-edge x-ray spectroscopy, where the polarizability is used to screen a highly-localized core-hole excitation. The advantage of the local, real-space approach is two-fold. First, it does not require the dense k -point grids of traditional reciprocal-space methods. Even for small unit

cells, a 2^3 k -point grid can be sufficient. Second, the size of the polarizability matrix is small and independent of the unit cell size. The formation of the screened Coulomb operator W from the polarizability involves several matrix operations that scale with matrix size to the third power. In the local, real-space approach the dimensions of these costly operations is minimized.

We revisit the local, real-space approach for two broad reasons: improvements to the accuracy of the calculations and improvements to the execution of the code. Highly accurate calculations are necessary to understand subtle changes in spectral features due to changes in crystal or electronic structure. First, we extend the calculation to include all-electron projectors and examine the effect of the pseudopotential approximation on the screened Coulomb potential. We find that pseudopotential-based wave functions yield an incorrect polarizability for small distances, *e.g.*, inside the pseudopotential radius. This is related to the removal of core-level electrons and hence nodes from the valence atomic orbitals, changing the density distribution of the valence orbitals. The discrepancy is small and limited to very near the atomic site, but has a noticeable effect on calculated near-edge x-ray absorption spectra which rely on the valence screening to determine the strength of exciton binding. Second, the calculation of the polarizability has been substantially rewritten to run in parallel as a hybrid OPENMP + MPI code, allowing screening calculations of large systems to be carried out quickly. Algorithmic improvements yield a scaling with system size of $N^2 \log N$.

In Section II, we review polarizability and screening and the main approximations of the real-space approach. In Section III, we detail how the use of pseudopotentials affects the orbitals near an atom which in turn modifies the electronic screening. The pseudopotential-based orbitals can be augmented, restoring the all-electron character, and we illustrate the effect this has on x-ray absorption calculations through modifications of the core-hole screening. In Section IV, we generalize the local, real-space approach for use in calculating valence (opti-

cal/UV) excitation spectra. In Section V, we detail the performance and scalability of our implementation, and we also note important algorithmic details that are general to calculations of the RPA polarizability. Finally, in Section VI, we explore convergence parameters and sources of error in this method before outlining the extension to a TD-DFT interaction kernel in Section VII and discussing future work in Section VIII.

II. REVIEW

A. Polarizability and Screening

We use Hartree atomic units throughout, such that the electron charge, electron mass, Planck's constant and Coulomb's constant are given by $e = m_e = \hbar = 4\pi\epsilon_0 = 1$. We make use of the one-electron Green's function

$$g^{-1}(1, 2) = g_0^{-1}(1, 2) - V(1, 2) - \Sigma(1, 2) \quad (1)$$

where each numerical index denotes position, time, and spin, g_0 is the non-interacting Green's function, V is the total potential, which is local and so contains a factor $\delta(1 - 2)$, and Σ is the self-energy encompassing many-body interactions.

The irreducible polarizability χ_0 of the electron system is simply the change in electron density n in response to a change in the potential V ,

$$\chi_0(1, 2) = \delta n(1)/\delta V(2). \quad (2)$$

The density can be written in terms of the one-electron Green's function

$$n(1) = -ig(1, 1^+), \quad (3)$$

where 1^+ refers to a time infinitesimally later than 1. Taking functional derivatives with respect to the potential in Eq. 1, the polarizability can be written

$$\begin{aligned} \chi_0(1, 2) &= -i\delta g(1, 1^+)/\delta V(2) \\ &= ig(1, 3)\frac{\delta g^{-1}(3, 4)}{\delta V(2)}g(4, 1^+). \end{aligned} \quad (4)$$

(We use the Einstein sum convention.) By approximating the Green's function using $g^{-1} = g_0^{-1} - V$, we arrive at the random phase approximation for the polarizability,

$$\chi_0^{\text{RPA}}(1, 2) = -ig_0(1, 2)g_0(2, 1^+). \quad (5)$$

This can be transformed from the two time representation to the response as a function of a single external energy.

Above, in Eq. 1, the potential term includes both the external and Hartree terms, and the Hartree term itself will change with changes in the electron density. One should therefore use the reducible polarizability χ which is the response to only changes in the external potential,

$$\chi = (1 - v\chi_0)^{-1}\chi_0 \quad (6)$$

written without obvious indices. Here v is the Coulomb potential. Most importantly, from the reducible polarizability one obtains the screened Coulomb interaction W resulting from some external potential v_{ext} ,

$$W = \epsilon^{-1}v_{ext} = v_{ext} + v\chi v_{ext}, \quad (7)$$

where ϵ is the dielectric function. This is central to many-body perturbation techniques, for instance, for treating single-particle self-energies via the GW method, or electron-hole excitation calculations via the BSE [12].

B. Local, Real-space Approach

The foundations of the local, real-space approach are twofold. First, the potential can be arbitrarily divided into pieces, allowing one to separately consider the screening of each piece. Second, at long distances, the dielectric screening simplifies from a matrix in coordinate-space to a single, frequency-dependent number, $\epsilon^{-1}(\mathbf{r}, \mathbf{r}', \omega) \rightarrow \epsilon^{-1}(\omega)$.

Following Ref. [1], the external potential, from either a core hole or a positive test charge at $\mathbf{r} = 0$, is divided into two regions by adding and subtracting a shell of charge:

$$\begin{aligned} v_{ext}(\mathbf{r}) &= v_1(\mathbf{r}) + v_2(\mathbf{r}), \\ v_1(\mathbf{r}) &= [v_{ext}(\mathbf{r}) + R_S^{-1}]\Theta[R_S - r], \\ v_2(\mathbf{r}) &= -R_S^{-1}\Theta[R_S - r] - r^{-1}\Theta[r - R_S]. \end{aligned} \quad (8)$$

Here Θ is the Heaviside theta function and R_S is the radius of the shell of charge. The external potential is assumed to be attractive (negative) and equal to $-r^{-1}$ outside R_S according to Coulomb attraction. It follows that one has

$$\begin{aligned} W &= \epsilon^{-1}v_{ext} \\ &= \epsilon^{-1}v_1 + \epsilon^{-1}v_2 \\ &= W^{(1)} + W^{(2)}. \end{aligned} \quad (9)$$

Because v_1 is nonzero only within R_S , the dielectric response that screens v_1 is also localized. In contrast, the screening of v_2 must still cover all space.

The utility of the local, real-space approach hinges on treating the screening of v_2 only approximately. First, regardless of the quality of the screening approximation, the importance of v_2 is controlled by the shell radius R_S , so that it entails a negligible, *controlled* approximation. As the radius is increased, v_2 goes to zero. The effect of dividing the calculation at finite R_S is addressed further in section VI C. A modified Levine-Louie dielectric model was adopted in Ref. [1] and is used here [13, 14]. The model screening is parametrized by the static, long-range dielectric constant ϵ_∞ and the average and local valence electron densities.

One weakness of this approach is that ϵ_∞ is treated as an input parameter. Small errors in ϵ_∞ (relative to the

true value of ϵ_∞) will only lead to small errors in the resulting x-ray absorption spectra, and we investigate this further in Sec. VID. However, this still assumes an input value for ϵ_∞ that is close to the true value. As suggested in Ref. [1], the preferred source is an experimental measurement of the optical constants or index of refraction below the band gap. In such cases where such data are not available, several computational approaches can be used. The optical spectra can be calculated with the OCEAN code [15, 16], either within the RPA or within the Bethe-Salpeter equation (BSE) approximation. For the latter, the dielectric constant is once again required, and several calculations might be necessary to converge the calculation such that the input static dielectric constant agrees with output one.

The short-ranged potential v_1 is screened by calculating the RPA polarizability. Typically we use a shell radius R_S between 3 a.u. and 5 a.u. The polarizability is calculated within a spherical region of space given by a radius of 8 a.u. to 10 a.u. Per Eq. 5, this necessitates calculating the one-electron Green's functions for this region of space. Improvements to the fidelity, efficiency, and parallelism of calculating g , χ_0 , and χ in order to screen v_1 are the focus of this work.

III. AUGMENTATION OF ELECTRON ORBITALS

A. Pseudopotentials

The screening method of Ref. [1], adopted in the OCEAN spectroscopy code, utilizes electron wave functions generated from a pseudopotential-based density-functional theory code. The pseudopotential approximation allows for a dramatic reduction in the computational cost of planewave codes. The core-level electrons are removed, and the Z/r potential of each ion is replaced by a pseudopotential, such that the valence electrons are the most-bound states. This reduces the computation cost in two ways: fewer electrons are treated, and the highly oscillatory parts of the electron wave functions are removed, reducing the required number of planewaves. More information on pseudopotential theory and methods can be found in [17]. We will attempt only an outline here.

Consider a pseudopotential V_{ion}^{ps} for an element which treat angular-momentum-dependent effects separably following the Kleinman-Bylander form [18]. For each value of the principle angular momentum l up to l_{max} it consists of some local potential and optionally some non-local projectors. In contrast, the all-electron ionic potential is simply an attractive Coulomb potential set by the ion's atomic number Z . Both the all-electron (ae) and pseudized (ps) radial Schrödinger equations can be

solved numerically.

$$\begin{aligned} H^{ae/ps} \phi_j^{ae/ps} &= \epsilon_j \phi_j^{ae/ps} \\ H^{ae/ps} &= -\frac{\nabla^2}{2} + \frac{l(l+1)}{2r^2} + V_H[n] + V_{xc}[n] + V_{\text{ion}}^{ae/ps} \end{aligned} \quad (10)$$

The Hartree V_H and DFT exchange-correlation V_{xc} potentials both depend on the density n , and so the problem must be solved self-consistently. Outside of some cut-off radius r_c the pseudopotential matches the all-electron ionic potential, and the pseudo and all-electron electron orbitals are equal for an isolated atom. At the cut-off additional smoothness requirements are enforced. The all-electron and pseudo orbitals should have the same first-derivatives and scattering length, although this is exact only for specific energies. Because the scattering properties are the same for the all-electron and pseudo wave functions, the behavior of the pseudo electrons in the interstitial regions is identical to that of the electrons in the all-electron system.

While pseudopotentials are capable of reproducing all-electron results for many properties, such as band structures (Bloch-state energies) or structural properties, they fall short in others, such as core-level excitations. This is unsurprising because there are no core-level electrons in the pseudo-potential system. We point to localization and location of a perturbation or transition operator in determining if the pseudopotential wave functions are sufficient. In the case of core-level transitions, the operator is both highly-localized and within the pseudized region. Conversely, structural properties are not localized. They rely on force constants, which are a measure of the change in the distribution electron density as felt by one atom in response to the motion of another. In the case of a real-space screening approach, we are interested in the density response to a localized perturbation, and for screening a core hole this localized perturbation is within the pseudized region.

To demonstrate the differences between an all-electron and pseudopotential screened core-hole, we can look at an isolated fluorine atom. In Fig. 1(a) we show the difference in the valence ($2s$ and $2p$) electron densities between the all-electron and the pseudopotential atomic systems. While the all-electron $2s$ orbital has a node (and is orthogonal to the $1s$ orbital), the pseudopotential $2s$ does not. The first antinode of the all-electron $2s$ is responsible for the difference in densities below around 0.2 a.u. Around 0.7 a.u. the pseudopotential density exceeds the all-electron density, a consequence of norm conservation and the deficiency at small radii. In Fig. 1(b) we plot the change in valence electron density upon introduction of a $1s$ core hole in the system. For both systems the valence electron density moves to smaller radii (towards the positively charged core-hole), but for the all-electron system there is a larger change at short distances. The situation is even more dramatic for heavier atoms, *e.g.*, in the case of iodine, the valence $5s$ and $5p$ orbitals have 4 and 3 fewer nodes in the pseudopotential system.

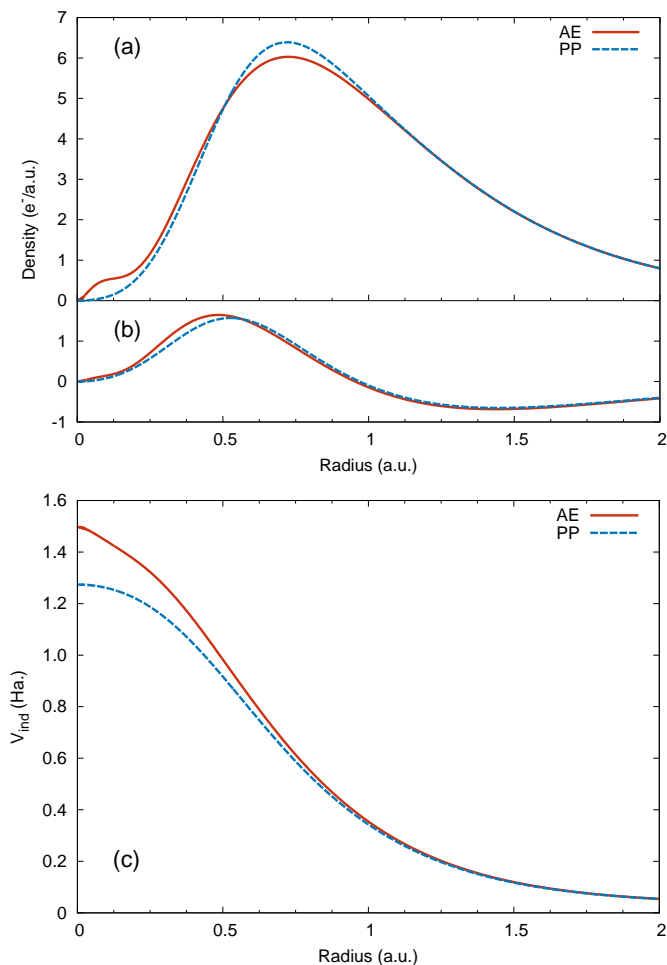


FIG. 1. (a) Valence electron density for an isolated fluorine atom for both the all-electron (AE, solid red) and pseudopotential (PP, dashed blue) systems. In the pseudopotential system the $2s$ orbitals have no nodes. This is why the all-electron systems has more density at very small radii, inside the $2s$ node at 0.2 a.u. (b) The change in valence density of the fluorine atom in response to a $1s$ core hole. (c) The induced potential that arises from the change in the valence density. Even though the difference in densities is quite small, the subsequent difference in the induced potential is substantial at short ranges.

The small difference in density response is magnified when converted into an induced potential as shown in Fig. 1(c). Clearly, at short distances the all-electron valence orbitals are more efficient at screening core-level excitations than the pseudopotential orbitals. In section IIID we will explore how this difference in induced potential affects calculated x-ray absorption spectra that can be compared to measured ones.

B. Optimal Projector Functions

To include the correct all-electron behavior, we augment wave functions of the pseudopotential system to

correct the *on-site* behavior. This augmentation style was introduced for core-level transitions in [15, 19] and is similar to the projector-augmented wave method [20]. By on-site we mean that projectors are only applied to the atom with the core hole. In contrast, complete augmentation would use projectors for every atom (pseudopotential) in the system. Augmentation exploits the same properties that we earlier asserted our pseudopotential would have. Namely, outside of the pseudopotential cut-off radius r_c the pseudo wave function is identical to the all-electron wave function. Over a reasonable energy range, a bound or scattering state can be transformed from the pseudopotential system to the all-electron system by replacing the pseudo wave function inside of the cut-off radius with the all-electron solution. In practice this is done by creating a set of projectors for both the all-electron and pseudized atomic systems which we refer to as the optimal projector functions (OPF). These projectors are chosen to be complete within the augmentation radius $r_a \geq r_c$ and within some energy window ε_{\min} to ε_{\max} .

The construction of the projectors is as follows. For each angular momentum l , self-consistent solutions to Eq. 10 are determined for both the all-electron and pseudo-potential systems, *e.g.*, for an isolated atom in either the ground-state or a positive ion such that the valence electrons are all bound. For this purpose, the desired energy window for the projectors is selected by choice. For each l , the energy of the most-bound valence state is found. In some cases this would be a semi-core state such as the $3s$ and $3p$ orbitals in titanium. The minimum energy is set below this bound state, $\varepsilon_{\min} = \varepsilon_v - \varepsilon_{\text{pad}}$, where the padding energy is 0.3 Ha. by default. The energy maximum is set to cover the relevant energy ranges, 50 eV to 100 eV for x-ray absorption transition matrix elements or 100 eV to 200 eV for RPA screening calculations (our default value is 5 Ha. ≈ 130 eV). Strictly speaking, this range depends on the Fermi energy and band gap, but for condensed-matter systems these values only vary by a few eV.

Having defined the system's effective Hamiltonians H^{ae} and H^{ps} and an energy window, we can begin to create the projectors. First, a set of pseudopotential partial waves are created for 128 energies spanning from ε_{\min} to ε_{\max}

$$H^{ps}\phi_i = \varepsilon_i\phi_i^{ps} \quad (11)$$

Note, the calculation is only carried out to a finite radius, and, therefore, there is no problem normalizing these states. Additionally, these states are not orthogonal, but instead provide an over-determined basis.

Next, for each pseudopotential partial wave ϕ_i^{ps} an all-electron partial wave ϕ_i^{ae} is also constructed. The ϕ_i^{ae} are not constructed to match exactly the energies of their corresponding pseudopotential partial wave, but instead to match the pseudopotential wave function and scattering properties. Specifically, we match the arctangent of the log-derivatives of the partial waves β , evaluated at the

augmentation radius r_a

$$\beta = \frac{r}{\phi} \frac{d\phi}{dr} \Big|_{r=r_a}$$

$$\bar{\delta} = \arctan[\beta] - \pi\eta \quad (12)$$

where η is the number of nodes in the partial wave, corrected for the lack of core-level resonances in the pseudopotential system. We will refer to $\bar{\delta}$ as the phase shift. The true phase shift can be related more carefully to the logarithmic derivative and the partial wave (see Sakurai Ch. 7 [21] among others). The pseudopotential properties, matching energy and smoothly matching the wave functions between the pseudo and all-electron systems, are only exact at specific energies. At other energies the mapping is only approximate, and we chose to enforce smoothness at the expense of the energy. As we are only interested in the spatial behavior of the augmented orbitals, this choice is natural.

Because we are matching phase shifts the energy of the all-electron partial wave is only approximately the same as that of the pseudopotential partial wave. A reference set of all-electron partial waves are constructed within the same energy window. Then the energy of each all-electron partial wave is iteratively refined until the phase shifts converge within 3×10^{-14} . Lastly, ϕ_i^{ae} is rescaled in a fashion that avoids numerical difficulties in cases of nodes and antinodes approaching r_a for a given energy:

$$\phi_i^{ae} := A_i \phi_i^{ps}$$

$$A_i = \frac{(\phi_i^{ps})^2 + (d\phi_i^{ps}/dr)^2}{\phi_i^{ps} \phi_i^{ae} + (d\phi_i^{ps}/dr)(d\phi_i^{ae}/dr)} \Big|_{r=r_a}. \quad (13)$$

Here the partial waves and derivatives are evaluated at the augmentation radius r_a . In the case where the partial waves and first derivatives are equal we have $A = 1$, whereas we typically find $0.95 \leq A \leq 1.05$.

We now have a set of all-electron and pseudopotential partial waves. To generate the optimal projectors we use principle-component analysis (PCA) [22]. We generate eigenvectors and eigenvalues of the overlap matrix S , with a matrix element and the k^{th} eigenvalue and eigenvector denoted by

$$S_{ij} = (\phi_i^{ps})^\dagger \phi_j^{ps}; \quad Sx_k = e_k x_k. \quad (14)$$

Using normalized partial waves the trace of S is the number of projectors $N \leq 128$. The eigenvectors are sorted by eigenvalues, and only a few with the largest eigenvalues are kept such that $\sum_k^n e_k > N(1-\iota)$, where n between 3 and 5 is usually sufficient for a small error ($\iota < 10^{-4}$). We can now construct the optimal projectors following the prescription,

$$p_k^{ae} = \sum_{i=1}^N x_{ki} \phi_k^{ae}; \quad p_k^{ps} = \sum_{i=1}^N x_{ki} \phi_k^{ps}. \quad (15)$$

Here both the pseudo and all-electron projectors are constructed from the same vector x_k . (In practice, we build

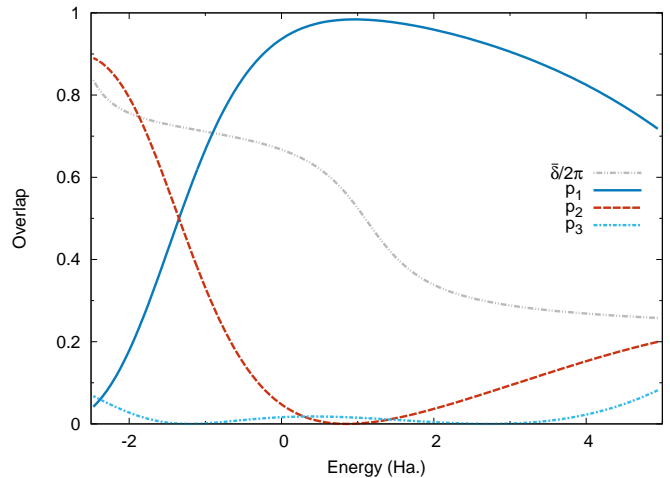


FIG. 2. Overlaps between $l = 0$ pseudopotential scattering states of titanium and the calculated OPFs as a function of the energy of the scattering state. For reference, the rescaled phase shift $\bar{\delta}/2\pi$ is plotted as well. Note the OPFs are not necessarily eigenstates for any energy, *i.e.*, the overlap for any single projector may be always less than 1.

the negative of S so that the eigenvalues with the largest absolute magnitude are also the lowest. We then only calculate 16 eigenvectors with the smallest eigenvalues using the SYEVR routine provided by the LAPACK library [23, 24].)

We call these projectors optimal because the PCA construction guarantees that the fewest projectors possible are chosen to span the space given by our set of partial waves and target error. The strength of this approach is that relatively few projectors per angular momentum are needed to span from the occupied valence bands through 130 eV above the Fermi level. The number of projectors generated is typically one more than the number of scattering resonances of spanned by the OPF energy window. In Figure 2 we show the overlaps between the partial waves and the optimal projectors $|\langle \phi_j^{ps} | p_i^{ps} \rangle|^2$ as a function of energy for the $l = 0$ states of titanium.

The augmentation of the electron wave functions is carried out using the projectors from Eq. 15. An all-electron wave function is given as follows (here μ denotes, say a Bloch state, and the atom's position is taken as the origin):

$$\psi_\mu^{ae}(\mathbf{r}) = \psi_\mu^{ps}(\mathbf{r})$$

$$+ \sum_{lm} \sum_j^{N_l} Y_{lm}(\hat{r}) \left(p_{jl}^{ae}(r) - p_{jl}^{ps}(r) \right) \langle Y_{lm} p_{jl}^{ps} | \psi_\mu^{ps} \rangle_{r_a} \quad (16)$$

where $-l \leq m \leq +l$, N_l is the number of projectors for a given angular momentum channel, and Y_{lm} are the spherical harmonics. The overlap between the wave function and the projectors is taken within the sphere defined by the with radius r_a . Further implementation details are given in Sec. V C.

C. Approximate augmentation

Previously, the OCEAN code relied on an approximation instead of carrying out augmentation of the wave functions. We document the old approach here, and in the next section we will compare it to the current method. As was shown in Fig. 1(c), even the isolated atom demonstrates the importance of all-electron wave functions when calculating the screening near the nucleus. The difference between the two induced potentials in Fig. 1(c) can be calculated purely within the isolated atomic case

$$\Delta v_{\text{ind}}(r) = v_{\text{ind}}^{ae}(r) - v_{\text{ind}}^{ps}(r). \quad (17)$$

Previously this correction was at times applied to the induced potential as calculated within the RPA using the *un-augmented* wave functions of the system. In this way the approximate effect of augmentation was included in the screening.

D. Screening with augmented orbitals

We now examine the effects of augmenting the orbitals used to calculate the RPA polarizability on calculations of near-edge x-ray absorption spectra (XAS). While augmentation has been previously used for interactions and matrix elements between core levels and valence or conduction levels [15], here we are interested in the effect on the spectra due to including augmentation in the calculation of the polarizability. Within the BSE approach, absorption spectra are modeled by considering an interacting electron-hole pair. The strong Coulomb attraction between the electron and the hole is screened by the dielectric response of the material. As we will show, the calculated XAS depends strongly on the strength of this attraction, and, therefore, the details of the screening.

We consider the halide K edges of lithium halides, LiF, LiCl, LiBr, and LiI. All crystallize in the rock salt $Fm\bar{3}m$ structure, and for all four materials a uniform core-hole lifetime broadening of 0.5 eV was used. Various convergence parameters are summarized in appendix B. The electron orbitals were calculated using the QUANTUM ESPRESSO code [25, 26] and the local-density approximation for the density functional [27]. Pseudopotentials are taken from PseudoDojo [28] and generated with ONCVSP [29]. We used the “high-accuracy” version of the lithium pseudopotential, which includes the Li 1s as valence. For bromine and iodine we use pseudopotentials including the *d* electrons: $3d4s4p$ and $4d5s5p$, respectively.

As an example, we first consider the fluorine K edge in LiF, which has been studied with OCEAN previously [15, 30]. Fig. 3 shows the effect of changes to the screened Coulomb attraction between the electron and core hole. In light grey, the non-interacting spectrum (neglecting electron-hole interactions) is dramatically different from

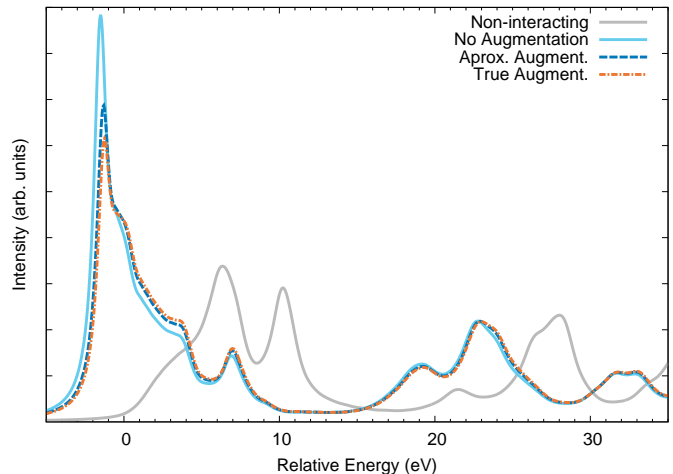


FIG. 3. The fluorine K-edge absorption in LiF using different approximations for the screened Coulomb interaction. Augmentation of the electron wave functions leads to a stronger screening of the core-hole potential. This stronger screening reduces the strength of the exciton and blue-shifts the spectra.

any other approximation, and it shows the importance of the excitonic binding on the absorption spectrum. The three different approximations to the screening all give qualitatively the same results, capturing a strong exciton around 1.5 eV below the onset of the non-interacting spectrum (0 eV in the plot). The differences are mostly confined to the near-edge region, within 10 eV of the onset. However, without augmentation the exciton is much too strong. Small changes in the relative strengths of near-edge features are also associated with structural disorder, *e.g.*, the pre-edge feature in LiF is a dipole-forbidden *s*-type exciton and can be observed with x-ray Raman scattering or due to finite-temperature disorder [15, 30, 31]. High-fidelity calculations are necessary for correctly identifying local structure.

Having shown the large effect of changes to the screening on the XAS of LiF, we next examine the effect of augmentation on heavier ions by exploring the range of lithium halides. In Fig. 4 we show the effects of different augmentation approaches on the halide K edges of LiCl, LiBr, and LiI. The trend between approximations for the same compound shown for LiF in Fig. 3 holds for the heavier halides as well. Calculating the screening of the core-hole potential with wave functions from a pseudopotential calculation dramatically under-screens the core hole, resulting in an exaggerated excitonic peak. There is a trend towards smaller discrepancy with increasing atomic number in the halide series. However, we conclude that the all-electron augmentation is necessary for the proper calculation of the screening even for heavier atoms. For Br and I, it appears that the approximate augmentation method may be sufficient. The differences are primarily confined to the near-edge region, which could be expected from Fig. 1(c). As for LiF, the differences between the augmented and un-augmented in-

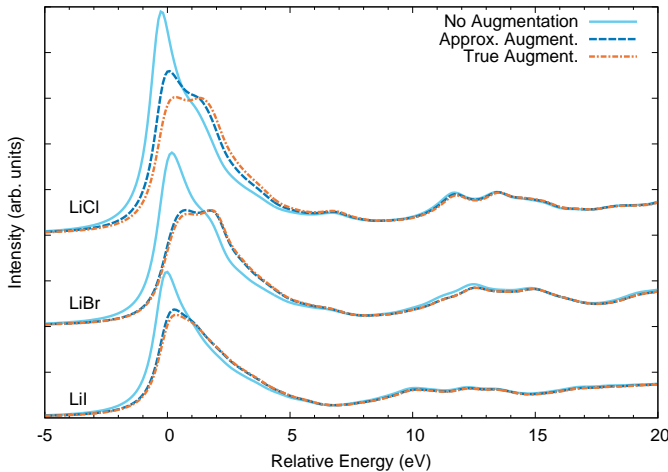


FIG. 4. The halide K-edge absorption for LiCl, LiBr, and LiI using different approximations for the screened Coulomb interaction. Across the three materials proper augmentation leads to increased short-range screening and weaker excitonic peaks.

duced potential are confined to a small region around the core hole. Only near the edge onset is the excited electron localized enough to be strongly affected by this very localized difference in core-hole potential. In addition, whereas the spectral weight at a given energy acquires contributions from higher energies (the non-interacting spectral features are pulled down by the core hole), it also should give up part of itself to lower energies.

Lastly, we examine the effects of augmentation by comparing calculations of LiI using two different iodine pseudopotentials. The standard iodine pseudopotentials uses a Kr core with the $4d$, $5s$, and $5p$ electrons in the valence bands while the semi-core pseudopotential also includes the $4s$ and $4p$ orbitals as valence. In Fig. 5 we show that the calculated I K edge of LiI does not depend on the pseudopotential when the orbitals are properly augmented for the screening calculation. However, without augmentation the screening calculated using the standard pseudopotential is notably weaker than that of the semi-core pseudopotential, leading to a stronger exciton. The weaker effect of augmentation on the calculation using the semi-core pseudopotential is due to the node in the $5s$ and $5p$ orbitals (absent for the standard pseudopotential). As discussed earlier (see Fig. 1), the absence of nodes in the pseudopotential orbitals shifts the electron density away from the atom. Even though without augmentation the $n = 5$ orbitals only get a single node in the semi-core system the effect is already dramatic and the discrepancy due to neglecting augmentation is strongly reduced.

We have demonstrated that the pseudopotential-based orbitals are insufficiently accurate for calculating the screened electron-hole interaction for core-level spectra. This failure is independent of the quality of the pseudopotential used. Instead it is a straightforward consequence

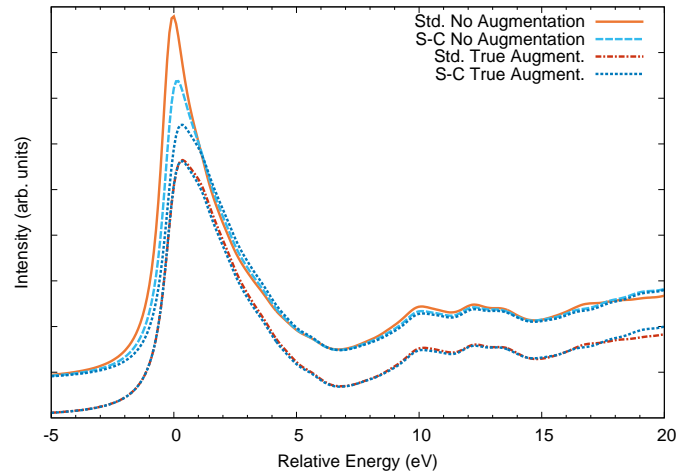


FIG. 5. The iodine K-edge absorption for LiI using either the standard (Std.) iodine pseudopotential ($4d5s5p$) or a semi-core (S-C) iodine pseudopotential ($4s4p4d5s5p$) and either no augmentation in the screening or true augmentation. The semi-core with true augmentation is plotted twice and the comparison between the two spectra with augmentation is displaced downward for clarity. With augmentation the two pseudopotentials give equivalent spectra.

of the difference in nodal structure between valence orbitals in the all-electron and pseudopotential systems. As shown in the atomic case (Fig. 1), the absence of nodes in valence orbitals of the pseudopotential system affects the density response and hence the screening. This is mitigated somewhat by the use of semi-core pseudopotentials that include the next highest principle quantum number in the valence, *e.g.*, Fig. 5.

Consider now the case of self-energy corrections via Hedin's GW method [32]. Here, the first-order many-body corrections to the one-electron Green's function are expressed as a product (integral over internal loop energy) of the Green's function G and the screened Coulomb operator W . The terms in the GW calculations are significantly less localized than core-level excitations, making discrepancies in the short-range part of W less important. However, in transition metals the d orbitals often drive important characteristics of the electronic behavior, forming the top of the valence bands, the bottom of the conduction bands, or both. From atomic calculations, it can be seen that the d orbitals overlap significantly with the semi-core orbitals of the same principle quantum number, *e.g.*, the $3d$ with the $3s$ and $3p$. High-accuracy calculations involving localized d orbitals may require accurately correcting the nodal structure of the s and p wave functions in much the same manner as we have shown for core-level spectroscopy. Several GW studies have pointed out discrepancies from using pseudopotentials [33] or excluding semi-core states [34, 35].

IV. SCREENING FOR VALENCE BSE

The OCEAN code is also capable of calculating valence optical/UV spectroscopy within the BSE, following earlier work [36, 37]. In moving from core-level to valence-level excitations, the hole is no longer confined to a local basis around the atom (the core-level orbital), but instead spans the unit cell. In OCEAN, the wave functions for the electrons and holes are sampled on regular real-space grids \mathbf{x} , and therefore we need a description of the screened Coulomb potential for each set of grid points $W(\mathbf{x}, \mathbf{x}')$. Previously, the screened potential was approximated using the Hybertsen-Levine-Louie dielectric model [13, 38], which depends parametrically on the local density $\rho(\mathbf{x})$ and static dielectric constant ϵ_∞ . Following Ref. [36], the screened Coulomb is given by,

$$W_{\text{HLL}}(\mathbf{x}, \mathbf{x}') = 1/2 [W_{\text{hom}}(|\mathbf{x} - \mathbf{x}'|; \rho(\mathbf{x}), \epsilon_\infty) + W_{\text{hom}}(|\mathbf{x} - \mathbf{x}'|; \rho(\mathbf{x}'), \epsilon_\infty)] \quad (18)$$

which simply averages the results using the density at points \mathbf{x} and \mathbf{x}' . To avoid the divergence at $\mathbf{x} \rightarrow \mathbf{x}'$, a spherical average over the discretization volume is used when $\mathbf{x} = \mathbf{x}'$.

To improve this, we substitute the more accurate local-RPA result for the short-range part of W . Using the previously introduced method, we can calculate the screened Coulomb from Eq. 9 for each grid point \mathbf{x} , ie, $W_{\mathbf{x}}$. Because the screening calculations are no longer guaranteed to be centered on atomic sites, we use un-augmented wave functions in the screening calculations. In the future, off-site augmentation can be added within the local, real-space scheme. At longer distances we fall back to the HLL model.

$$W(\mathbf{x}, \mathbf{x}') = \begin{cases} \frac{1}{2} [W_{\mathbf{x}}(\mathbf{x}') + W_{\mathbf{x}'}(\mathbf{x})], & \text{if } |\mathbf{x} - \mathbf{x}'| \leq r_m \\ W_{\text{HLL}}(\mathbf{x}, \mathbf{x}'), & \text{otherwise} \end{cases} \quad (19)$$

As above, we use the average to enforce the symmetry in interchanging \mathbf{x} and \mathbf{x}' . The transition radius r_m governs the transition between the two approximations.

Like the HLL model, care must be taken when evaluating the real-space W in the limit of $\mathbf{x} \rightarrow \mathbf{x}'$. We numerically integrate the $l = 0$ component of the calculated screened potential over the discretization volume V_x , the unit cell volume divided by the number of grid points,

$$W_{\mathbf{x}}(\mathbf{x}) = \frac{3}{R_x^3} \int_0^{R_x} W_{\mathbf{x}}(r) r^2 dr, \quad (20)$$

where $R_x = [3V_x/4\pi]^{1/3}$.

The system-size scaling behavior is the same for the valence screening as it was for the core-level case — the number of grid points \mathbf{x} scales linearly with volume the same as the expected number of atomic sites. (The scaling is discussed in section V and illustrated in V G.) There are two major differences between calculating the

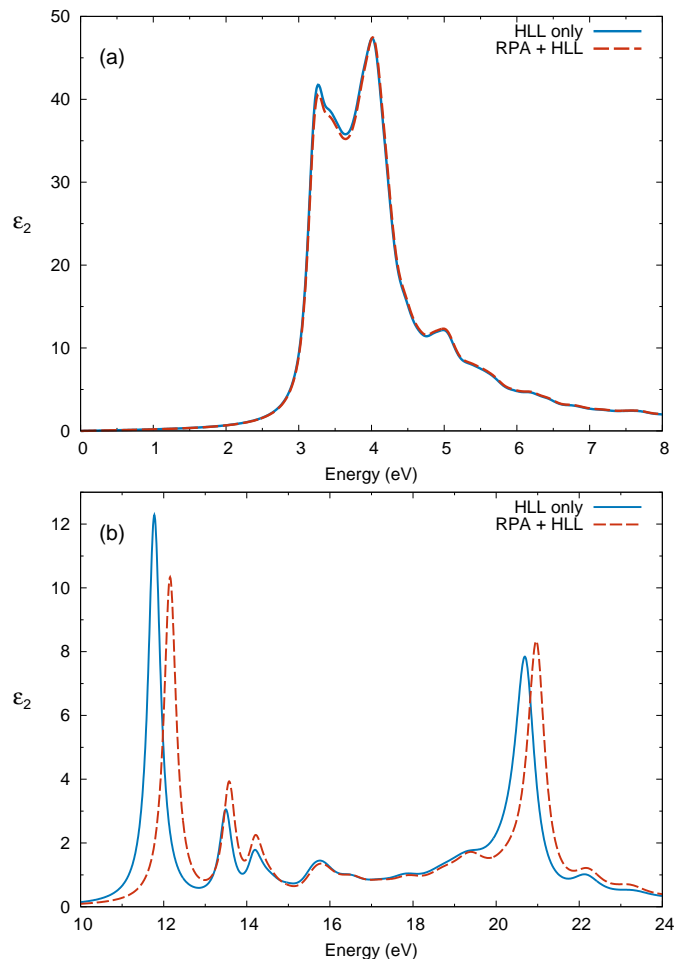


FIG. 6. The imaginary part of the dielectric function for silicon (a) and LiF (b) as a function of energy. The spectra are generated using two different approximations to the screened Coulomb interaction W . The Hybertsen-Louie-Levine model dielectric is given by the solid, blue lines, while those using the local, real-space RPA are dashed, red lines.

screening for the valence and core cases with negative and positive impacts on run time. First, the number of real-space grid points is much larger than the number of atoms. For example, in a unit cell of LiF an 8^3 x-point mesh is necessary, resulting in 512 screening sites instead of the 1 needed for the fluorine x-ray absorption calculation. The dramatic increase in sites is offset by the use of coarser real-space grids. The perturbing potential for the core case is the core-hole potential, and, like the core hole's density, it is strongly localized. In the valence case, the perturbing potential is taken to be a uniform ball of charge whose volume is set by the discretization volume V_x defined above. Therefore, the valence screening calculations converge with a coarser radial mesh than is needed for the core-level screening.

To showcase the effects of using the local RPA instead of the HLL screening on valence calculations we consider calculations of the imaginary part of the dielectric function for a range of systems.

First, we look at bulk silicon — the standard for valence electronic structure calculations providing a testbed for early DFT, GW , and valence BSE calculations [39]. As for the lithium halides we use the experimental lattice constant of 0.543 nm [40] and the PseudoDojo pseudopotential for silicon. Additional input parameters are included in appendix B. A scissor correction was used to set the DFT band gap to be 1.11 eV [41]. Unsurprisingly, we see in Fig. 6(a) that in the case of silicon the HLL model performs very well. The inclusion of the RPA screening at short range has little effect on the spectrum of bulk silicon.

Next we return to LiF (also well studied previously within the BSE [15, 42, 43]). The simulation details are similar to the x-ray case, but we have included a scissor correction to set the DFT band gap to 14.2 eV [44]. In contrast to bulk silicon, LiF is strongly ionic with the valence orbitals primarily localized on the fluorine site, making it a more difficult system for the model. In Fig. 6(b), we see a substantial discrepancy between the HLL-only and RPA results. Both the main exciton near 12 eV and the higher energy peak near 21 eV are red-shifted in the HLL as compared to the RPA+HLL calculation. This shift indicates that the HLL model screening is weaker than the RPA calculation for these two peaks. This is consistent with a larger GW band-gap correction that often occurs with the HLL approximation is used as compared to when the RPA is used [45].

V. IMPLEMENTATION WITHIN OCEAN

As previously stated, our goal is to calculate the screened Coulomb interaction, starting from the irreducible polarizability within the RPA (Eq. 5). There are a number of costs and bottlenecks associated with this calculation. To review, the screened Coulomb interaction W is directly calculable from the reducible polarizability χ . The calculation of χ involves matrix products and matrix inversions of the Coulomb operator and the irreducible polarizability χ_0 . Within the RPA, χ_0 follows from the one-electron Green's function g , which itself can be written from the the electron orbitals. In this Section, we will explicitly outline the algorithms used in version 3 of OCEAN [15, 16], and we will examine the scaling behavior with system size and parallel performance.

A. Electron wave functions and local basis

The initial step is determining the electron wave functions and the basis, from which we can generate the Green's functions. Density-functional theory (DFT) is used to simulate the electronic Hamiltonian. The system is taken to be periodic such that the electron orbitals can be denoted by their band n , crystal momentum \mathbf{k} , and spin σ ,

$$H^{\text{DFT}}\psi_{n\mathbf{k}\sigma} = \psi_{n\mathbf{k}\sigma}\varepsilon_{n\mathbf{k}\sigma}, \quad (21)$$

where each wave function $\psi_{n\mathbf{k}\sigma}$ has energy $\varepsilon_{n\mathbf{k}\sigma}$. The Green's function for energy E can be written in the spectral representation

$$g_{\sigma}(\mathbf{r}, \mathbf{r}', E) = \sum_{n=1}^{\infty} \int_{\text{BZ}} \frac{d^3\mathbf{k}}{(2\pi)^3} \frac{\psi_{n\mathbf{k}\sigma}^{\dagger}(\mathbf{r})\psi_{n\mathbf{k}\sigma}(\mathbf{r}')}{E - \varepsilon_{n\mathbf{k}\sigma}} \quad (22)$$

The integral runs over the Brillouin zone.

To construct g we must define the real-space basis. As mentioned in Sec. II B, we calculated the RPA response only for the local potential v_1 . We employ a real-space basis within a sphere S with a radius r_S and centered on a point τ . For screening the core hole, τ is the atomic site, while for valence calculations τ is one of the grid points in Eq. 19. The irreducible polarizability $\chi_0^{(\tau)}$ is then an $N_r \times N_r$ size matrix, as are the Green's functions $g^{(\tau)}(E)$. This real-space basis is independent of the size of the system's unit cell, and is discussed further in Sec. VI A 1.

In practice the sum over bands is truncated, and the integral is replaced with a sum over regularly spaced points in k -space. Our approach requires only a few k -points, often between 1 and 8, and we address this later in section VI B on errors and convergence. The sum over bands, however, is significant. Typically, convergence in the screening is reached when the Green's function is constructed with states up to around 100 eV above the Fermi level. This requires on the order of 30 to 50 bands per atom, and the number of bands required scales linearly with system size. Unfortunately, aspects of the generation of the one-electron states from DFT scale with the square of the number of bands.

B. Projecting the wave functions

After initialization, the first task in calculating the screening is that the Kohn-Sham orbitals must be converted. The external plane-wave DFT program has already diagonalized the DFT Hamiltonian for some set of points in reciprocal space (k -points). These eigenstates ψ are saved to file as Bloch states u ,

$$\psi_{b\mathbf{k}}(\mathbf{r}) = e^{i\mathbf{k}\cdot\mathbf{r}}u_{b\mathbf{k}}(\mathbf{r}) = e^{i\mathbf{k}\cdot\mathbf{r}}\sum_{\mathbf{G}}C_{b\mathbf{k}}(\mathbf{G})e^{i\mathbf{G}\cdot\mathbf{r}} \quad (23)$$

which are defined in terms of complex-valued coefficients C of plane waves \mathbf{G} . The eigenstates are sorted by energy, starting at the lowest or most-bound, and are indexed by b . The spin index σ will be dropped. Only the set of coefficients C , not the various phases, are written to file. We will use bars to indicate when a process has only a subset of the total indices, *e.g.*, bands \bar{b} or k -points $\bar{\mathbf{k}}$. We distribute the work for the conversion by band and k -point — not by plane wave coefficient. This limits the parallelization to $N_{\text{cpu}} \leq N_{\mathbf{k}}N_b$.

To project the wave functions onto our spherical grid, we can follow the method given by Eq. 23 directly, *i.e.*, Fourier interpolation. We first create a matrix of the

phases, as these will be common across all of the bands at a specific \mathbf{k} -point.

$$P_{\mathbf{k}}(\mathbf{r}, \mathbf{G}) = e^{i(\mathbf{k}+\mathbf{G})\cdot\mathbf{r}} \quad (24)$$

$$\psi_{\mathbf{k}}(\mathbf{r}, \bar{b}) = \sum_{\mathbf{G}} P_{\mathbf{k}}(\mathbf{r}, \mathbf{G}) C_{\mathbf{k}}(\mathbf{G}, \bar{b}) \quad (25)$$

where the bar indicates that we are processing only a subset of the total number of bands. The phase matrix requires $\mathcal{O}[N]$ operations from the plane waves, regardless of the number of processors included. Projecting the wave functions is $\mathcal{O}[N^2]$ from the plane waves and bands, but the bands are distributed by processor. The summation over \mathbf{k} -points is not counted in the estimation of computational cost because it decreases with volume and is usually 8 or 1. For a system with more than one site of interest, *e.g.*, a disordered, liquid, or amorphous system, the number of sites, and therefore the number of local real-space grids, increases with volume as well. This means that the actual costs increase to N^2 and N^3 .

As an alternative we can use a fast Fourier transform (FFT), followed by interpolation, and completed by applying a complex phase:

$$\begin{aligned} u_{\bar{b}\mathbf{k}}(\mathbf{x}) &= \mathcal{F}\mathcal{F}\mathcal{T}[u_{\bar{b}\mathbf{k}}(\mathbf{G})] \\ u_{\bar{b}\mathbf{k}}(\mathbf{r}) &= \text{Interp.}[u_{\bar{b}\mathbf{k}}(\mathbf{x})] \\ \psi_{\bar{b}\mathbf{k}}(\mathbf{r}) &= e^{i\mathbf{k}\cdot\mathbf{r}} u_{\bar{b}\mathbf{k}}(\mathbf{r}). \end{aligned} \quad (26)$$

The real-space grid \mathbf{x} is defined as the Fourier transform dual of \mathbf{G} . The costs, including a factor of N sites, are $\mathcal{O}[N^2 \log N]$, $\mathcal{O}[N^2]$, and $\mathcal{O}[N^2]$, respectively. All three steps are independent over bands, \mathbf{k} -points, and spins, providing good scaling with the number of processors.

To determine the break-even point between these two methods we must be more specific with the actual costs of each step. The N^3 term from method 1 is $N_{\mathbf{G}} N_b N_{\mathbf{r}} N_i$, where i are the atomic sites. The $N^2 \log N$ term from method 2 is $A_F N_{\mathbf{G}} N_b \log N_{\mathbf{G}}$, where A_F is the FFT prefactor. Therefore, method 2 is preferable if $A_F \log N_{\mathbf{G}} < N_{\mathbf{r}} N_i$. Under the assumption that the logarithm of even a large number is about 10, method 2 is likely preferable, even for single-site calculations [46].

While an FFT is faster than the naïve Fourier transform of Eq. 23, the FFT does not directly give the wave functions on the desired radial grid. An interpolation step is used to move from the FFT grid \mathbf{x} to the radial grid \mathbf{r} . We have implemented a 4th-order Lagrange polynomial interpolation which is assisted by oversampling the FFT. The number of Fourier components is increased, $N_{\mathbf{G}} \rightarrow 8 \times N_{\mathbf{G}}$ ($2 \times$ in each dimension), with the added coefficients set to 0. The actual size of the FFT grid is increased further to generate a grid whose constituent primes are 2 through 7 — a 7-smooth number, but with an option to include a single factor of either 11 or 13. The interpolants are cached, allowing reuse between points both within the \mathbf{r} -grid for a single site as well as across sites. We make use of the FFTW3 library when available [47]. More sophisticated methods

for Fourier interpolation onto *irregular* grids have been proposed in literature, *e.g.*, [48] and references therein.

C. Augment

The next step is augmenting the wave functions to recreate the all-electron character,

$$\begin{aligned} \psi_{b\mathbf{k}}^{ae}(\mathbf{r}) &= \psi_{b\mathbf{k}}^{ps}(\mathbf{r}) \\ &+ \sum_{\nu,l,m} Y_{lm}(\hat{r}) [\phi_{\nu l}^{ae}(\mathbf{r}) - \phi_{\nu l}^{ps}(\mathbf{r})] \langle \phi_{\nu l}^{ps} Y_{lm} | \psi_{b\mathbf{k}}^{ps} \rangle, \end{aligned} \quad (27)$$

where ϕ are the OPFs and Y_{lm} are spherical harmonics. In the case of screening core-hole potentials, this is simplified because the local basis has the same origin as the projectors.

To carry out the augmentation, first the OPFs are projected onto the same real-space basis as the wave functions by linear interpolation. The local basis is substantially coarser than that used in the construction of the OPFs. Therefore we enforce unitarity by constructing the overlap matrix A ,

$$A_{\nu\nu';l} = \int_0^{r_a} dr r^2 \phi_{\nu l}^{ps}(r) \phi_{\nu' l}^{ps}(r), \quad (28)$$

where any deviation from the identity matrix is due to errors from using a coarser grid. The augmentation of Eq. 27 is modified,

$$\begin{aligned} \psi_{b\mathbf{k}}^{ae}(\mathbf{r}) &= \psi_{b\mathbf{k}}^{ps}(\mathbf{r}) \\ &+ \sum_{lm} \sum_{\nu,\nu'} Y_{lm}(\hat{r}) [\phi_{\nu l}^{ae}(\mathbf{r}) - \phi_{\nu l}^{ps}(\mathbf{r})] A_{\nu\nu';l}^{-1} \langle \phi_{\nu' l}^{ps} Y_{lm} | \psi_{b\mathbf{k}}^{ps} \rangle, \end{aligned} \quad (29)$$

preserving unitarity. Each process stores a copy of the OPFs and carries out the augmentation for its subset of bands and \mathbf{k} -points.

D. Building g and χ_0

The RPA polarizability from Eq. 5 can be transformed from the two-time form to a convolution over energy, which can be carried out along the imaginary axis,

$$\begin{aligned} \chi_0(\mathbf{r}, \mathbf{r}', \omega = 0) &= -i \sum_{\sigma} \int_{-\infty}^{\infty} \frac{dE}{2\pi} g_{\sigma}(\mathbf{r}, \mathbf{r}', E) g_{\sigma}(\mathbf{r}', \mathbf{r}, E) \\ &= \sum_{\sigma} \int_{-\infty}^{\infty} \frac{dt}{2\pi} g_{\sigma}(\mathbf{r}, \mathbf{r}', \mu + it) g_{\sigma}(\mathbf{r}', \mathbf{r}, \mu + it) \end{aligned} \quad (30)$$

where μ is chosen to be in the middle of the gap for insulators or at the Fermi level in metals to avoid poles in g . (With minimal approximation, a small energy Δ can be added in quadrature in metals to the difference between μ and the Kohn-Sham eigenvalue $\varepsilon_{b\mathbf{k}}$ according to $(\mu - \varepsilon_{b\mathbf{k}}) \rightarrow \pm \sqrt{(\mu - \varepsilon_{b\mathbf{k}})^2 + \Delta^2}$. This same approach can be used for calculating the dynamic polarizability,

$\omega \neq 0$. However, additional care is needed to avoid the poles in Green's function $g(\omega + \mu + it)$ as $t \rightarrow 0$. The integral is replaced by a sum over an energy grid as outlined later in Sec. VIA 2.

From the previous step, the electron wave functions are stored as $\psi_{\bar{\mathbf{k}}}(\mathbf{r}; \tau)$ where each processor might have only a subset of bands b and k-points \mathbf{k} , but all of the real-space points \mathbf{r} for all sites τ . The irreducible polarizability, as written in Eq. 30 is an integral over internal energy of the product of two Green's functions. The Green's functions require a sum over all k-points and bands. The spin, which has so far been ignored, does not get summed at this point, and spin-up and spin-down one-electron Green's functions can be treated separately. In principle, partial Green's functions could be constructed with the current, band and k-point distributed wave functions. However, it is more efficient to redistribute the wave functions into blocks by \mathbf{r} and site. The processors are split into groups such that each group works on its own site or set of sites. Within each group, the processors divide up the \mathbf{r} -points. This means that the wave functions are now distributed as $\psi_{b\mathbf{k}\sigma}(\bar{\mathbf{r}}; \bar{\tau})$.

$$g_{\sigma}^{(\tau)}(\bar{\mathbf{r}}, \bar{\mathbf{r}}', \mu + it) = N_k^{-1} \sum_{\mathbf{k}} \sum_{b=1}^{N_b} \frac{\psi_{b\mathbf{k}\sigma}^{\dagger}(\bar{\mathbf{r}}) \psi_{b\mathbf{k}\sigma}(\bar{\mathbf{r}}')}{\mu + it - \varepsilon_{b\mathbf{k}\sigma}} \quad (31)$$

where \mathbf{r} implicitly includes only the points for site τ . If background communications are enabled, the majority of this data transfer takes place while the conversion process is on-going. Within a group of processors cooperatively working on a site $g^{(\tau)}$, the wave functions are shared.

An important consideration in efficiently calculating the Green's function is that it involves an outer-product of the wave functions. For each band and k-point, N_r inputs are turned into N_r^2 outputs, with $2N_r^2$ operations. In a typical, small calculation the real-space grid has 1600 points per site, which means that at each frequency the Green's function is just under 40 MB in size, making it too large to fit in the local cache of a typical modern processor. A naïve implementation would require moving the Green's function to and from main memory for each band and k-point in the summation. This would limit the speed of the calculation because of limited memory bandwidth. Instead, the wave functions are broken up, and the Green's function is calculated by tiles. By default, each tile is 16×16 , such that it takes up 4 kB of memory (assuming 16 byte complex numbers), which is smaller than a typical 32 kB L1 cache. Precise tuning would depend on the specific underlying hardware.

E. Construct χ and W

In the previous step, we calculated the irreducible polarizability χ^0 . The reducible polarizability is given by

$$\chi = [1 - \chi^0 v]^{-1} \chi^0, \quad (32)$$

where v is the Coulomb potential operator. We do this by projecting into a spherical basis

$$\chi^0(\mathbf{r}, \mathbf{r}') = \sum_{lm} \sum_{l'm'} \chi_{lm;l'm'}^0(r, r') Y_{lm}(\hat{r}) Y_{l'm'}^*(\hat{r}') \quad (33)$$

$$v(\mathbf{r}, \mathbf{r}') = \sum_{lm} \frac{4\pi}{2l+1} \frac{r_{<}^l}{r_{>}^{l+1}} Y_{lm}(\hat{r}) Y_{lm}^*(\hat{r}') \quad (34)$$

where the Coulomb operator is diagonal in l, m . We can define

$$S_{lm;l'm'}(r, r') = \delta_{l,l'} \delta_{m,m'} \delta(r - r') - \int dx x^2 \chi_{lm;l'm'}^0(r, x) \frac{4\pi}{2l'+1} \left[\frac{r_{<}^{l'}}{r_{>}^{l'+1}} \right]_{x, r'} \quad (35)$$

by taking advantage of the diagonal nature of v in this basis. We therefore have

$$\chi_{lm;l'm'}(r, r') = S_{lm;l'm'}^{-1}(r, r'') \chi_{l'm'';l'm'}^0(r'', r'), \quad (36)$$

which requires one to consider the entire matrix S which has dimension $N_r(N_l + 1) \times N_r(N_l + 1)$.

In this basis the induced change in electron density from the short-range part of the core-hole potential $v^{(1)}$ is

$$\rho^{\text{ind}}(\mathbf{r}) = \sum_{lm} \rho_{lm}^{\text{ind}}(r) Y_{lm}(\hat{r}) \quad (37)$$

$$\begin{aligned} \rho_{lm}^{\text{ind}}(r) &= \sum_{l'm'} \int d^3 r' \chi_{lm;l'm'}(r, r') v^{(1)}(r') Y_{l'm'}(\hat{r}') \\ &= \int dr' r'^2 \chi_{lm;00}(r, r') v^{(1)}(r') \end{aligned} \quad (38)$$

The perturbing (core-hole) potential is taken to be spherical and therefore only the $l' = 0$ part of χ contributes. Giving a final, induced potential

$$\begin{aligned} v^{\text{ind}}(\mathbf{r}) &= \sum_{lm} v_{lm}^{\text{ind}}(r) Y_{lm}(\hat{r}) \\ v_{lm}^{\text{ind}}(r) &= \int dr' r'^2 \rho_{lm}^{\text{ind}}(r') \frac{4\pi}{2l+1} \frac{r_{<}^l}{r_{>}^{l+1}}. \end{aligned} \quad (39)$$

By default, only the $l = 0$ part of the response is calculated, according to

$$\begin{aligned} \bar{\chi}(r, r') &= S_{00;00}^{-1}(r, r'') \chi_{00;00}^0(r'', r') \\ \bar{\rho}^{\text{ind}}(r) &= \int dr' r'^2 \bar{\chi}(r, r') v^{(1)}(r'). \end{aligned} \quad (40)$$

The resulting induced potential is approximately the same as the $l = 0$ component of the full induced density $\bar{\rho} \approx \rho_{00}$. For the core-hole potential, the strong localization means that $l = 0$ component of the induced potential is dominant, and this approximation is reasonable.

F. Γ -point

There is an additional consideration for large unit cells. When only a single k -point is required, the electron orbitals can be calculated at the Γ -point. For systems with time-reversal symmetry the Bloch functions can be treated as real (instead of complex). This results a reduction of the required storage by half and substantial time savings in the DFT stage. A smaller reduction in runtime is also realized in the screening calculation as shown below in Table I.

G. Timing and Scaling

The calculation of the screening as outlined here is dominated by three steps: calculating the wave functions, projecting them onto the radial grid, and constructing the Green's function and χ^0 . The first, calculating the electron orbitals using DFT, is carried out using the QUANTUM ESPRESSO code [25, 26]. We report the timing of the DFT step for completeness, however, we are focused on the two steps that are specific to our screening calculation.

To investigate the timing and scaling of screening calculations within OCEAN we use LiF (physical details and convergence parameters were given in Sec. III D). There are two classes of scaling that we are interested in. First there is system scaling, by which we mean the increase in run time with an increase in the system size. This highlights the inherent simulation size limits of our approach. We will also consider strong scaling, the change in execution time due to changing the number of processors. We have implemented two levels of parallelism for the screening calculations: internode MPI and shared memory OPENMP. The testbed for these calculations is a small cluster with 12 nodes. Each node has a dual-socket with 8 processors per CPU (16 per node) [49]. Each timing run was repeated 8 times, and the average value is reported (DFT calculations were run only once).

For the tests, we consider various supercells of LiF, from the unit cell $N_F = 1$, to an $6 \times 8 \times 8$ supercell $N_F = 384$, covering cell volumes from 110 a.u.³ to 42000 a.u.³ (6.2 nm³). For these runs, 32 bands per unit cell were included (12288 for $N_F = 384$). For each supercell the screened Coulomb potential is calculated for all the fluorine sites. Each local real-space grid had 2624 points, and the Green's functions were evaluated at 16 imaginary frequencies.

First we look at the scaling with system size or weak scaling. In Fig. 7 we show the run time of the projection (ψ) and construction of the Green's function and polarizability (g & χ) steps as a function of super cell size. In this set of runs only Γ -point sampling of the Brillouin zone was used. The times are rescaled by dividing by N_F^2 and normalized to the timing of the $N_F = 64$ run. The $\approx \mathcal{O}[N^2]$ growth in calculating the screening is evident by the flat plots, though overhead or inefficiencies factor

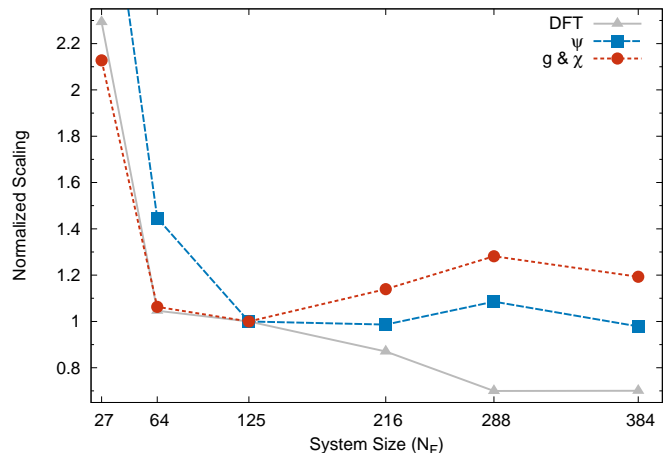


FIG. 7. The normalized run time for the screening given by dividing the run time by the square of the system size, normalized to the timing of $N_F=125$. The screening is divided into the wave function projection ψ (blue, squares) and construction of the Green's function and polarizability G & χ (red, circles). For the DFT calculation (grey, triangles) the scaling is normalized by the system size cubed. The un-normalized data are included in the top section of Table I.

into the timing of the smallest run. We also include the timing of the DFT run, but rescaled by N_F^3 . 128 processors across 8 nodes were used for every run, using 128 MPI processes.

The timing information for the range of systems from $N_F = 1$ to $N_F = 384$ is shown in Table I. To give a full picture of the scaling, three different settings for the k -point sampling were used: finite sampling on a 2^3 k -point mesh, single k -point sampling, and Γ -point sampling. Above $N_F = 27$, a single k -point is sufficient to sample the Brillouin zone and gives the same results as the 2^3 sampling (but more quickly). The purpose of timing single k -point runs in addition to the Γ -point runs is to distinguish the changes due to the reduction in k -point sampling from 8 to 1 from the changes in moving between complex and real Bloch functions. In contrast to the Γ -point runs, the single k -point is taken at $(1/8, 2/8, 3/8)$.

Next, we present the change in run time with changing processor number or strong scaling, (Fig. 8). Ideally, doubling the number of processors used in a calculation will halve the runtime. Longer than expected runtimes may result from serial sections of the code or communication overhead. Shorter than expected times may result from better data caching due to each processor working on a smaller data set. Here we plot the data as the efficiency E as a function of the number of processors N ,

$$E(N) = \frac{N_0}{N} \frac{t(N_0)}{t(N)} \times 100\% \quad (41)$$

where the efficiency is normalized to the run time with N_0 processors. Ideal scaling is given by an efficiency of 100%. The efficiency is the measure of merit for planning high-throughput calculations. In high-throughput

N_F	Vol. (a.u. ³)	k -pts	DFT (s)	ψ (s)	g & χ (s)
384	42002	Γ	27421.6	333.6 (8.4)	1474 (22)
288	31502	Γ	11556.1	208.1 (4.5)	891.0 (14.6)
216	23626	Γ	6063.4	106.4 (3.0)	445.7 (5.2)
125	13673	Γ	1350.2	36.1 (0.1)	131.0 (1.5)
64	7000	Γ	189.6	13.7 (0.1)	36.5 (1.1)
27	2953	Γ	31.2	5.36 (0.02)	13.0 (0.4)
<hr/>					
125	13673	1	2791.2	92.0 (1.0)	166.1 (3.6)
64	7000	1	609.5	79.9 (0.2)	57.0 (5.1)
27	2953	1	62.5	30.3 (0.1)	15.6 (0.5)
8	875	1	6.0	9.36 (0.41)	1.28 (0.04)
<hr/>					
64	7000	8	4585.4	175.5 (5.2)	425.4 (72.9)
27	2953	8	408.6	45.8 (1.0)	128.0 (4.7)
8	875	8	17.9	17.5 (0.3)	9.86 (0.03)
1	110	8	0.2	4.39 (0.11)	0.46 (0.04)

TABLE I. Timing in seconds of selected LiF runs, denoted by the number of fluorine atoms and the k -point sampling (k -pts) running on 128 processors (see text). The DFT timing includes only the “electron” time for the non-self-consistent run to generate the wave functions for the screening. The two divisions of the screening calculation, labeled ψ and g & χ , encompass the totality of the runtime for the screening. The timing for ψ includes the time to read in the wave functions, project and augment them, and redistribute them. The timing for g & χ includes the time to construct the Green’s functions, evaluate the polarizability, and screen the core-hole potential. The root-mean-square deviations were determined over 8 repeated runs and are included in parentheses.

calculations the available hardware resources can be divided between many different calculations, and the runtime of any single calculation should be balanced against the runtime of the complete dataset.

In Fig. 8 we show that for a moderately sized system $N_F = 64$, there is a drop-off in efficiency above 16 processors. In part this is a reflection of the structure of our computer cluster, where each addition of 16 processors increases the number of nodes in the calculation by 1. While the efficiency is quite poor running on 160 processors, the runtime is also very brief. The average time is 41.1 sec. compared to an idea time of 27.3 sec. The larger systems show better scaling.

Lastly, we examine the OMP parallelism by repeating the Γ -centered calculations and including thread-level parallelism. The total number of processors was held fixed at 128, but divided between MPI and OMP. We repeat the Γ -point weak-scaling test for 2, 4, and 8 OMP threads per MPI process. The results are shown in Table II. We find relatively uniform performance across the four different processor arrangements, but a drop-off in performance using 8 OMP threads. This drop-off indicates an opportunity for further code refinement to better support higher-levels of OPENMP parallelism.

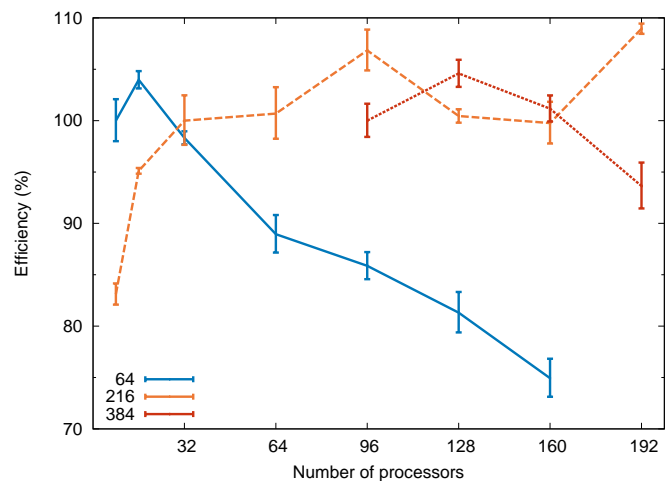


FIG. 8. The strong scaling behavior of the complete screening calculation for three different systems sizes, $N_F = 64$ (solid, blue) normalized for 8 processors, $N_F = 216$ (dashed, orange) normalized for 32 processors, and $N_F = 384$ (dotted, red) normalized at 96 processors. The error bars reflect the root mean square deviation determined by averaging over 8 runs. We see a fall-off in efficiency of the smaller system, but for $N_F = 216$ and $N_F = 384$ we see good strong scaling up to 192 processors.

VI. GRIDS, CONVERGENCE, AND ERRORS FROM APPROXIMATIONS

A. Grids and Integrals

As outlined previously in Sec. V on the implementation within OCEAN, the Green’s functions are calculated on a real-space grid determined by separate radial and angular grids, and the internal energy loop integral is calculated for a set of imaginary energies.

1. Radial and angular grids

The real-space points used for calculating the Green’s functions and polarizability are constructed from separate radial and angular grids

$$\mathbf{r}_i = r_j \otimes \hat{\Omega}_k \quad (42)$$

The angular grids are taken from the set of extremal points by Womersley and Sloan [50]. For a given degree n each angular grid has dimension $(n + 1)^2$. The radial grid has two options, uniform spacing or Gauss-Legendre quadrature. Uniform spacing has the advantage that it is directly equivalent to a plane-wave energy cutoff $|\mathbf{G}_{\max}| = \pi/\Delta r$. However, testing indicates that the quadrature grids are more efficient, generating converged results with fewer points. The radial space can be divided into arbitrary parts, each with its own grid spacing or quadrature grid.

N_F	MPI	OMP	ψ (s)	g & χ (s)
384	128	1	333.6 (8.4)	1474 (22)
	64	2	330.9 (11.6)	1488 (15)
	32	4	336.4 (2.6)	1430 (31)
	16	8	504.5 (19.3)	1452 (49)
288	128	1	208.1 (4.5)	891.0 (14.6)
	64	2	204.2 (4.9)	898.1 (33.0)
	32	4	210.4 (2.1)	767.4 (5.7)
	16	8	315.0 (12.6)	775.8 (6.0)
216	128	1	106.4 (3.0)	445.7 (5.2)
	64	2	105.8 (2.1)	447.1 (9.3)
	32	4	108.7 (5.4)	465.9 (28.4)
	16	8	167.3 (2.1)	423.6 (7.4)
125	128	1	36.1 (0.1)	131.0 (1.5)
	64	2	35.4 (1.0)	151.7 (2.9)
	32	4	34.3 (0.2)	148.0 (7.2)
	16	8	53.6 (0.7)	157.4 (13.3)
64	128	1	13.7 (0.1)	36.5 (1.1)
	64	2	11.6 (0.1)	37.4 (0.8)
	32	4	12.4 (1.7)	38.6 (4.1)
	16	8	16.3 (0.1)	40.6 (4.4)
27	128	1	5.36 (0.02)	13.0 (0.4)
	64	2	2.88 (0.01)	8.4 (0.5)
	32	4	2.69 (0.36)	10.4 (1.7)
	16	8	3.35 (0.02)	12.2 (0.3)

TABLE II. Timing in seconds of LiF runs with Γ -point sampling. A total of 128 processors are used for each run divided between MPI tasks and OPENMP threads. The two timing sections are the same as in Table I.

By default, we divide the space in two using r_a , the augmentation radius from the OPFs. Within this radius we use a 16-point Gauss-Legendre radial grid and the 36-point ($n = 5$) angular grid. The dense radial grid captures the behavior of the all-electron reconstructed wave functions close to the atomic site. For the section outside r_a , we use a uniform grid such that $(r_{\max} - r_a)/N < 0.45$ a.u., typically 16 points, and the angular grid is increased to 64 points ($n = 7$). This gives the Green's functions and polarizability dimensions of 1600×1600 , independent of the size of the unit cell.

2. Energy integration

By construction, the RPA polarizability requires an integral over the internal loop energy. As shown in Eq. 30 this can be transformed from an integral over real energies to one over complex energies by closing the contour and realizing that above the Fermi energy all of the poles (single-particle excitation energies) are displaced below the real axis by a small imaginary component. Likewise, below the Fermi level the poles are displaced above the

real axis. Therefore, the contour is closed by arcs in the upper-right and lower-left quadrants and does not encompass any poles. The Green's function is relatively smooth at imaginary values, and we use quadrature to replace the integral with a summation over relatively few energy points.

Following Ref. [1], we first divide $t \in (-\infty, \infty)$ into four regions, symmetric across $t = 0$ by the parameter ζ . such that the number of quadrature points in the region $(0, \zeta)$ will be the same as within (ζ, ∞) . This allows Eq. 30 to be rewritten as

$$\begin{aligned} \chi_0 &= \sum_{\sigma} \int_{-\infty}^{\infty} \frac{dt}{2\pi} g_{\sigma}(\mathbf{r}, \mathbf{r}', \mu + it) g_{\sigma}(\mathbf{r}', \mathbf{r}, \mu + it) \\ &= \sum_{\sigma} \frac{\zeta}{\pi} \int_0^1 da \left[g_{\sigma}(\mathbf{r}, \mathbf{r}', \mu + i\zeta a) g_{\sigma}(\mathbf{r}', \mathbf{r}, \mu + i\zeta a) \right. \\ &\quad \left. + a^{-2} g_{\sigma}(\mathbf{r}, \mathbf{r}', \mu + i\zeta/a^2) g_{\sigma}(\mathbf{r}', \mathbf{r}, \mu + i\zeta/a^2) \right] \end{aligned} \quad (43)$$

The parameter ζ is chosen to be the geometric mean of the largest and smallest values of $|\mu - \varepsilon_{b\mathbf{k}}|$, *i.e.*, half the band gap and the larger of the distance from μ to the bottom of the valence bands or the top of the conduction bands. To prevent ζ from going to zero in metallic systems, 0.5 eV is added in quadrature to the minimum (half-gap) value.

The integral over a in Eq. 43 is replaced by a summation over quadrature points. The energy points a_i and weights w_i are taken from GaussLegendre quadrature, shifted and scaled by half to match the range. Quadrature grids from 4 to 64 points are implemented in the code. In Ref. [1], it was suggested that the two-part integrand be replaced with a single product of Green's functions with energy points at $i\zeta a/(1-a)$ with a prefactor of $(1-a)^{-2}$, giving

$$\begin{aligned} \chi_0 &\approx \sum_{\sigma} \sum_i^{N_i} \frac{\zeta w_i}{\pi(1-a_i)^2} g_{\sigma}(\mathbf{r}, \mathbf{r}', \mu + i\frac{\zeta a_i}{1-a_i}) \times \\ &\quad \times g_{\sigma}(\mathbf{r}', \mathbf{r}, \mu + i\frac{\zeta a_i}{1-a_i}). \end{aligned} \quad (44)$$

This reproduces the correct large and small a behavior of Eq. 43, but with only a single set of quadrature points. Using this single-grid approximation, a 16-point quadrature grid was found to be sufficient. For systems with time-reversal symmetry, the spatial indices on one of the Green's functions can be interchanged. This allows us to calculate only a single Green's function and square it.

B. Bands and k -points

The convergence of the screening calculation also depends on the number of k -points and bands included in the Green's functions. The convergence behavior with respect to bands is similar in our approach and other sum over states methods. A large number of unoccupied

bands may be required, and the error falls as the inverse of the number of bands [51]. To generalize between materials it is preferable to speak of the energy range of the unoccupied bands included in the calculation, *e.g.*, the average energy of the highest-band with respect to the conduction band minimum. In Fig. 9(b) we show the convergence of the screening potential of the fluorine 1s hole in LiF with respect to the energy range of unoccupied states. This is done by plotting the difference between the calculated induced potential using a conduction band range of 200 eV and that calculated with smaller ranges, *e.g.*, $\Delta v_{ind}[100 \text{ eV}] = v_{ind}[200 \text{ eV}] - v_{ind}[100 \text{ eV}]$, etc. Typically, the induced potential near the core hole increases with an increase in the number of bands included in the screening calculation.

Like the summation over bands, the k -point sampling should also be infinite. However, while the summation over bands takes the place of an energy integral whose upper bound is positive infinity, the summation over k -points is, by construction, a properly normalized discretization of the volume integral over the Brillouin zone. Errors in finite k -point sampling arise when the electron wave functions at a given momentum are a poor approximation of other points within the discretization volume. In the real-space approach, the convergence with k -points is rapid. Even for systems with small units cells like LiF, only a few k -points are required. In Fig. 9(c) we show the difference plots from reducing the k -point sampling from 4^3 down to 3^3 and 2^3 . With only a $2 \times 2 \times 2$ k -point grid, the errors in the induced potential are less than 10 mHa.

C. Real-space Truncation

As introduced in Sec. II B, the real-space approach relies on partitioning the space around the core hole (or test charge). This partitioning is carried out in Eq. 8, where a spherical charge of radius R_S neutralizes the long-range Coulomb tail, allowing the RPA screening to be carried out only locally. Our approximation doesn't change the total external potential that is screened. However, by using a model dielectric to calculate $W^{(2)}$ we introduce differences with respect to a calculation using the RPA polarizability everywhere. Having previously outlined the effect of neglecting the core-hole potential and the effects of various approximations to the augmenting the pseudopotential wave functions in the previous section, we now look to the influence of R_S on the calculated screened core-hole potential and subsequently the absorption spectrum.

To assess the effects of finite R_S on the calculated screened potential we compare the induced potential for the fluorine K edge of LiF. In Fig. 9(d) we show the induced potential calculated with a shell radius of 6 a.u. and the difference in the potentials between those calculated with shell radii of 5 a.u., 4 a.u., and 3 a.u.: $\Delta v_{ind}[R_S=5] = v_{ind}[R_S=6] - v_{ind}[R_S=5]$. Near the fluorine site, the difference between the induced poten-

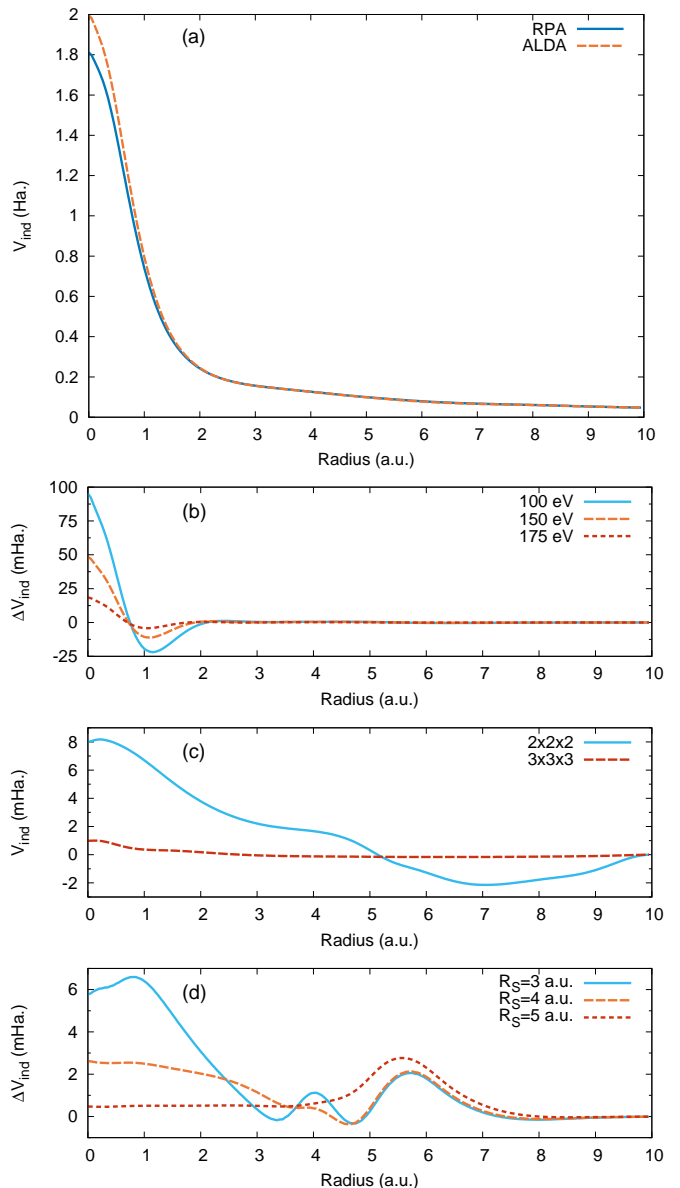


FIG. 9. a) The induced potential in response to a fluorine 1s hole in LiF calculated using a shell radius of 6 a.u. and 120 conduction bands, spanning approximately 200 eV, and a 4^3 k -point sampling (solid, blue). The orange, dashed line shows the induced potential calculated using f_{xc} within the adiabatic LDA (see text sec. VII). b) The difference plots obtained by subtracting the induced potential calculated with different numbers of bands. c) The difference plots for changing k -point grids. d) The difference plots for the induced potential changing only the sphere radius R_S . Note that the difference plots are in mHa.

tial at $R_S = 6$ a.u. and $R_S = 5$ a.u. is less than 0.013 eV, while the maximum difference between the two, located at 5.55 a.u. (approximately the length of a lattice vector), is less than 0.076 eV.

D. Long-range Dielectric Constant

As mentioned previously, the static long-range dielectric constant ϵ_∞ is a required input for our local, real-space approach. The error near the core hole due to an incorrect dielectric constant is approximately

$$\Delta W \approx \left(1 - \frac{1}{\epsilon_\infty}\right) R_S^{-1} - \left(1 - \frac{1}{\widetilde{\epsilon}_\infty}\right) R_S^{-1} \quad (45)$$

where $\widetilde{\epsilon}_\infty$ is the input dielectric constant. This can be expressed in terms of percentage error in the input dielectric constant

$$\Delta W \approx \frac{1}{\widetilde{\epsilon}_\infty R_S} \left(\frac{\epsilon_\infty - \widetilde{\epsilon}_\infty}{\epsilon_\infty} \right). \quad (46)$$

As an example, for $\epsilon_\infty = 5$, $R_S = 5$ a.u., a 10 % underestimation ($\widetilde{\epsilon}_\infty = 4.5$) would lead to an error of 0.12 eV. This absolute error directly affects calculations of chemical shifts using the OCEAN code [52].

To showcase the errors from an incorrect input value of ϵ_∞ we look at FeS₂ in the cubic *Pnnm* phase marcasite. As before the cell parameters are taken from experiment [53], the pseudopotentials were taken from PseudoDojo, specifically the “high-accuracy” iron potential, and further input parameters are listed in the appendix. Absent a previously calculated or experimentally measured value for the static dielectric constant, the input ϵ_∞ can be determined self-consistently as shown in Fig. 10. We find that an input value of $\epsilon_\infty = 25$ results in a BSE calculation of approximately the same value (25.06) with the photon momentum vector aligned along (111). Unsurprisingly, the strength of the static dielectric constant effects the calculated dielectric response, but even comparing $\epsilon_\infty = 10$ to $\epsilon_\infty = 50$ the spectra are in qualitative agreement.

Next we can compare this effect on the x-ray edges of FeS₂ in Fig. 11. Neither the sulfur K edge nor the iron L edge are strongly dependent on the input value of the dielectric constant. The energy scale of both is relative to the conduction band minimum of the $\epsilon_\infty = 10$ calculation (of the L₃ edge of iron). The slight shifts in the onset of the $\epsilon_\infty = 25$ and $\epsilon_\infty = 50$ spectra are due to changes in the excitonic binding and core-level shift due to differences in the input dielectric. As can be seen in Fig. 11, for x-ray absorption calculations it may be sufficient to have only a rough estimate of the dielectric constant.

VII. BEYOND RPA SCREENING

From a many-body perturbation theory perspective, the RPA is the lowest-order diagram for the polarizability. Higher-order approaches could consider interactions between the electron and hole lines in the RPA, or, equivalently, a vertex correction. One such vertex correction is given by the adiabatic local-density approximation (ALDA). As shown by Del Sole, Reining, and Godby

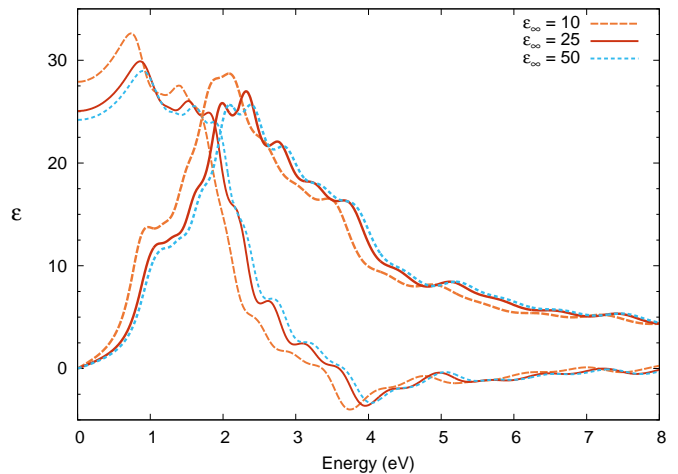


FIG. 10. The real (thin) and imaginary (thick) components of the complex dielectric constant of FeS₂ plotted for 3 different inputs of the static dielectric constant ϵ_∞ . If the value of ϵ_∞ is not known from prior calculations or experiment, valence BSE calculations can be carried out to determine it self-consistently: $\epsilon_\infty = 25$.

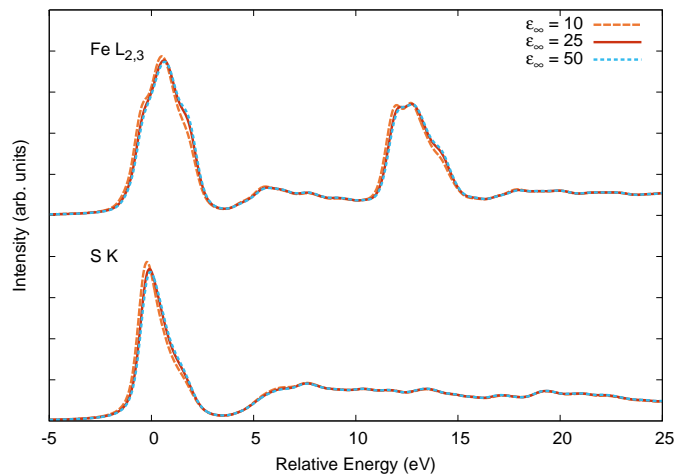


FIG. 11. For FeS₂ marcasite, the Fe L_{2,3} edge and S K edges are plotted for 3 different inputs of the static dielectric constant ϵ_∞ . Despite large differences in the input ϵ_∞ , the spectra are largely unchanged. The relative positioning takes into account the changes in the effect of the changing screened core-hole potential on the chemical shifts (see text). The error in the position of either edge is less than 0.13 eV for $\epsilon_\infty = 10$.

[54], if the first-order approximation to the one-electron self-energy is taken to be the local exchange-correlation potential

$$\Sigma(1, 2) = \delta(1, 2)v_{xc}(1) \quad (47)$$

then the reducible polarizability (and screened interaction W) undergo a relatively simple transformation. Re-

peating Eq. 6,

$$\begin{aligned}\chi &= (1 - v\chi_0)^{-1} \chi_0 \\ \tilde{\chi} &= (1 - (v + f_{xc})\chi_0)^{-1} \chi_0\end{aligned}\quad (48)$$

where f_{xc} is the derivative of the exchange-correlation potential with respect to the density, $f_{xc}(1,2) = \delta v_{xc}(1)/\delta n(2)$, and $\tilde{\chi}$ is the ALDA polarizability. The use of an ALDA kernel has been investigated within the *GW* approximation [54–56] and for valence BSE calculations of small molecules [57].

Within the ALDA, f_{xc} is a contact interaction, and the expression in Eq. 48 is easily evaluated using the OCEAN code as outlined in section VE. In the real-space basis f_{xc} is diagonal and can be written

$$f_{xc}(\mathbf{r}, \mathbf{r}') = \delta(\mathbf{r} - \mathbf{r}') \left. \frac{dv_{xc}(n)}{dn} \right|_{n=n(\mathbf{r})} \quad (49)$$

where v_{xc} is the LDA exchange-correlation potential and is evaluated at the density n at position \mathbf{r} . The electron density $n(\mathbf{r})$ is taken from the initial DFT calculation used to generate the electron orbitals for the screening. We start with the Perdew-Zunger parameterization for the exchange [58] and Vosko, Wilk and Nusair parameterization of the correlation energy [59] within the local-density approximation fit to the data of Ceperley and Alder [60]. We calculate f_{xc} directly as the second derivative of the exchange-correlation energy with respect to the density using a 5-point finite difference using density differences of $0.01 e^-$ per a.u.³. Spin-polarized calculations beyond the RPA are not yet supported, but can be included using this same scheme.

Once again looking at LiF, we can examine how calculating the polarizability with the ALDA instead of RPA changes the XAS. As shown in Fig. 9(a), the induced potential including f_{xc} is significantly stronger. This in turn leads to a weaker core-hole potential and correspondingly weaker excitonic effects. The effect of including f_{xc} in the screening calculation is more pronounced than the changes due to convergence parameters shown in sections VIB and VIC. In Fig. 12 we show the fluorine K-edge XAS using both approximations for the screening. The BSE spectrum calculated using the ALDA is substantially different from the RPA result, but only in the near-edge region within 10 eV of the onset. The small differences at higher energies would be hidden by broadening if the calculation included the effects of the electron self-energy and vibrational disorder.

While the only vertex correction implemented in OCEAN is the ALDA, an extension to semi-local exchange-correlation kernels is straightforward, requiring only the additional knowledge of the density gradients. Because f_{xc} is formed explicitly in real-space, the formulation of Eq. 48 is also compatible with non-local exchange-correlation potentials. This would require construction of f_{xc} as a real-space matrix instead of the diagonal form (Eq. 49). By construction the response is

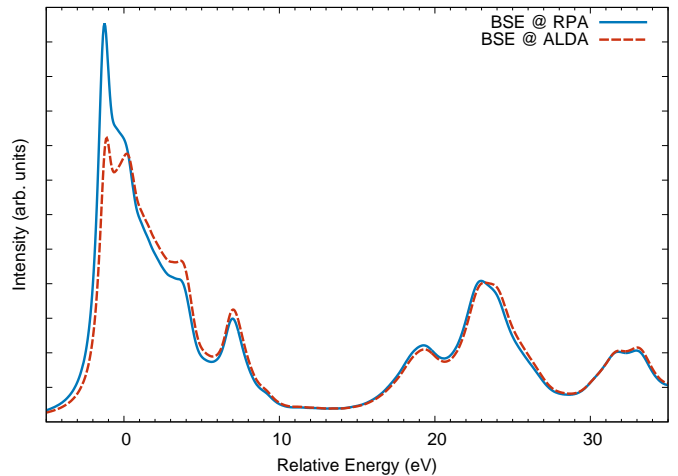


FIG. 12. The F K-edge absorption for LiF calculated using BSE, but two different approximations to calculate the screening. The adiabatic LDA (ALDA) approximation screens the core hole much more efficiently [see Fig. 9(a)] resulting in significantly less excitonic binding. Compared to the RPA results, the ALDA has a weaker exciton and a general shift of spectral weight to higher energies.

still localized and in response to a local perturbing potential with the long-range response handled by a model. Therefore, any non-local f_{xc} must be of limited range.

VIII. DISCUSSION AND FUTURE DIRECTIONS

We have presented an efficient and scalable method for calculating the RPA polarizability of condensed systems. The method scales well with system size N , increasing only by $N^2 \log N$. While the method is limited to calculating the full RPA response within a restricted real-space range, it is coupled with a model dielectric function. This approximation is controlled through a radial cutoff R_S , and the contribution of the model goes smoothly to zero as $R_S \rightarrow \infty$. This method is implemented within the OCEAN code where the screened Coulomb operator W is used as part of the BSE Hamiltonian for calculating both core-level (near-edge x-ray) and valence-level (UV/vis) spectroscopy.

We conclude with a few remarks on improvements and future directions. The relative ease of the local, real-space method may present an opportunity for developing and testing new model dielectric functions and easily benchmarking them against an RPA or TD-DFT quality calculations. Additionally, by calculating only a localized response function, vertex corrections beyond the ALDA of Section VII are still inexpensive to apply. In the remainder of this section we briefly touch on a few possible enhancements to the method as well as other computations beyond particle-hole spectroscopy that could benefit from our local, real-space polarizability.

A. Refinements

In the current implementation there is no re-use of the Green's functions between sites. The use of site-centered radial grids makes it unlikely that a given $(\mathbf{r}, \mathbf{r}')$ pair of one site will exist in the grid of another. However, it is reasonable to expect that many point pairs will be close to shared, *e.g.*, for sites α and β that $\mathbf{r}_\alpha \approx \mathbf{r}_\beta$ and $\mathbf{r}'_\alpha \approx \mathbf{r}'_\beta$. In the future, the construction of the grids can be relaxed to maximize the overlaps, decreasing the computational cost of generating the Green's functions. This would be especially helpful in the case of valence calculations where the site density is high.

Future improvements to the scalability with system size must focus on generating the electron wave functions. For medium to large system sizes, most of the time is spent in calculating the screening in the DFT (see Sec. V G). This is exacerbated by the need for unoccupied states in calculating the Green's function. Several methods have been proposed to reduce the number of unoccupied states.

One option is to directly replace part of the sum over unoccupied states. The effective-energy techniques replace the energy denominator in the sum over unoccupied states [61–63]. The completeness of the Bloch functions then allows the sum over unoccupied bands to be replaced with the identity minus a sum over occupied bands. However, these approaches differ in two main ways from ours, not including our local approximation. First, the energy convolution is carried out analytically, and the RPA polarizability is constructed via sums over states. In our approach the Green's functions are built via a sum over states and the convolution is carried out numerically. Second, the effective-energy approaches are formulated in reciprocal space, which has the advantage of a straightforward approximation for the effective energy. An easier alternative would be to approximate the neglected bands as plane waves [64–66].

Alternatively, the induced density response and therefore the screened potential can be more directly calculated using the linear-response Sternheimer equation approach [6, 67] or eigenvalue decomposition of the polarizability matrix [7, 68]. While these approaches only require the occupied orbitals, they maintain an unfavorable N^4 scaling with system size. Better scaling might be achievable by adapting these approaches to determine only the local response.

B. Non-BSE Applications

The screened Coulomb interaction W has many uses in calculations of condensed matter systems other than the use presented here of the direct interaction in the BSE. One such application is in self-energy calculations

using the GW method which requires evaluating the self-energy operator,

$$\Sigma(\mathbf{r}, \mathbf{r}', E) = i \int \frac{d\omega}{2\pi} G(\mathbf{r}, \mathbf{r}', E - \omega) W(\mathbf{r}, \mathbf{r}', \omega) \quad . \quad (50)$$

The local screening approach outlined here can be used to efficiently generate W with RPA quality for small distances $|\mathbf{r} - \mathbf{r}'|$. In the present approach only static screening was implemented. However, the contour integral in Eq. 30 can be modified to calculate $\omega \neq 0$, and the fundamental scaling of frequency-dependent screening remains the same as that of the static case. In addition to standard valence- and conduction-band self-energy calculations, an adaptation of this method could be applicable for determining accurate core-level binding energies [69].

A second type of calculation for which the local, real-space screening might be useful is phonon calculations. Within the harmonic approximation, the phonons of a system can be fully described by the dynamical matrix. The elements of the dynamical matrix are proportional to the derivative of the force on atom a with respect to changes in the position of a' . This is equivalent to the second derivative of the total energy with respect to the displacement of both. The elements of the dynamical matrix can be calculated using density-functional perturbation theory [70–72]. Alternatively, the dielectric response can be used since the polarizability describes how the electron density will change in response to a change in the potential, in this case the motion of the atomic nuclei. Care is required as the polarizability gives the density change in response to a local perturbing potential, but standard pseudopotentials include non-local terms [73].

Appendix A: Model polarization

Here we reproduce the model screening of a spherical shell of charge by the model dielectric function introduced in [14] as used in [1]:

$$\chi_M(\mathbf{r}, \mathbf{r}') = -(2\rho_0)^{-1} \times \quad (A1) \\ \times \nabla \cdot \nabla' [\rho(\mathbf{r}) + \rho(\mathbf{r}')] B(|\mathbf{r} - \mathbf{r}'|),$$

where ρ is the local electron density and ρ_0 is the average electron density. The real-space model B is the transform of the Levine-Louie dielectric model $B(q)$.

$$B(|\mathbf{r} - \mathbf{r}'|) = \int \frac{d^3q}{(2\pi)^3} B(q) \exp[i\mathbf{q} \cdot (\mathbf{r} - \mathbf{r}')] \quad (A2)$$

$$B(q) = \frac{1}{4\pi} \left(\frac{1}{\epsilon_{LL}(q; \rho_0, \epsilon_\infty)} - 1 \right). \quad (A3)$$

The original formulation of the Levine-Louie model in Ref. [13] requires something akin to an average band gap, but this can be reformulated using the long-range dielectric constant ϵ_∞ .

$$\epsilon_{\text{LL}} = 1 + \frac{2}{\pi q_F} \left[\frac{1}{Q^2} - \frac{\lambda}{2Q^3} \left(\tan^{-1} \left[\frac{2Q + Q^2}{\lambda} \right] + \tan^{-1} \left[\frac{2Q - Q^2}{\lambda} \right] \right) \right] + \left(\frac{\lambda^2}{8Q^5} + \frac{1}{2Q^3} - \frac{1}{8Q} \right) \ln \left(\frac{\lambda^2 + (2Q + Q^2)^2}{\lambda^2 + (2Q - Q^2)^2} \right) \quad (\text{A4})$$

where $Q = q/q_F$, $\lambda^2 = (\epsilon_\infty - 1)^{-1} \omega_p^2 \omega_F^{-2}$, ω_p is the plasmon frequency, and ω_F and q_F are the Fermi frequency and wave vector of a non-interacting electron gas of density ρ_0 .

Appendix B: Input parameters for x-ray and optical calculations

We consider the halide K edges of lithium halides, LiF, LiCl, LiBr, and LiI. All crystallize in the same rock salt $Fm\bar{3}m$ structure with lattice constants of 0.4017 nm, 0.5130 nm, 0.5501 nm, and 0.6000 nm, respectively [40]. The plane-wave cut-off energy was set to 100 Ry. (increased to 120 Ry. for the bromine and iodine pseudopotentials), and the density was converged using a 4^3 shifted k -point grid. The BSE final states were solved on a 15^3 grid (16^3 for LiI), including 32, 59, 127, or 128 unoccupied bands, respectively, and were downsampled onto a 12^3 real-space mesh (10^3 for LiF). The calculations used the local-density approximation for the density functional [27], and pseudopotentials are taken from PseudoDojo [28] and generated with ONCVSP [29]. The DFT calculations were carried out using QUANTUM ESPRESSO [25, 26]. We used the “high-accuracy” version of the lithium pseudopotential, which includes the Li $1s$ as valence. For bromine and iodine the standard $3d4s4p$ ($4d5s5p$) were used, and additional calculations were carried out with the semi-core iodine pseudopotential. Note that no valence-level spin-orbit coupling is considered, which would affect the Br $4p$ or I $5p$ states.

For the screening calculations of the lithium halides, the orbitals for the screening calculation were generated on a 4^3 k -point grid, including 72, 150, 197, or 213 bands, for F, Cl, Br, and I respectively, such that energy range from the Fermi level (mid gap) to the highest unoccupied state was approximately 150 eV for each. The augmentation radius of each was set by the pseudopotential of each halide, 1.64 a.u., 1.76 a.u., 1.97 a.u., and 2.02 a.u., respectively, and 1.45 a.u. for the I semicore. For the heavier three the polarizability was calculated within a sphere of radius 8 a.u. on a 160-point uniform radial grid

and 64-point angular grid while the neutralizing shell was placed at $R_S = 4$ a.u. For the LiF the polarizability was calculated within a sphere of radius 10 a.u. with the neutralizing shell placed at $R_S = 6$ a.u. The real-space grid was divided into three sections. The inner section used a 34-point Gauss-Legendre quadrature for the radial grid and a 64-point angular grid. From the augmentation radius of 1.64 a.u. to 2.96 a.u. a 27-point, uniformly spaced radial grid and 144-point angular grid was used, and the final grid was an 88-point, uniformly spaced radial grid and 256-point angular grid. This grid is excessive for calculations of spectra, but was chosen to accurately show the convergence effects in Fig. 9.

For the valence calculations, both the LiF and Si used a 8^3 real-space grid for the BSE final states, requiring RPA screening calculations on that grid. For LiF, the polarizabilities were calculated within a sphere of radius 8 a.u. on a 80-point uniform radial grid, a 64-point angular grid, and the neutralizing shell was placed at $R_S = 4$ a.u. For Si the radial grid was reduced to 40 points and the shell was placed at 3.5 a.u. For the LiF valence calculations BSE final states were calculated on a 16^3 k -point mesh. The RPA screening for the valence used a 2^3 k -point mesh and 72 bands. Silicon crystallizes in a $Fd\bar{3}m$ structure with experimental lattice constant 0.543 nm [40]. The PseudoDojo pseudopotential for silicon and a planewave cut-off of 100 Ry were used. The BSE final states were calculated on a 16^3 k -point grid, including 8 conduction and 4 valence bands. For the RPA screening 200 bands on a 2^3 k -point mesh were used.

Marcasite crystallizes in the cubic $Pn\bar{3}m$ phase. The lattice parameters were set to 0.44446 nm by 0.54246 nm by 0.33864 nm to match experiment [53]. A planewave cut-off of 100 Ry was used and the density was converged on a 4^3 k -point mesh. The “high-accuracy” iron and standard sulfur pseudopotentials were taken from PseudoDojo. The BSE final states were solved on a $12 \times 10 \times 16$ k -point mesh, including 72 unoccupied bands, and downsampled onto an $8 \times 10 \times 6$ real-space mesh. For the screening calculations a 2^3 k -point mesh and 200 bands were used.

* john.vinson@nist.gov

¹ E. L. Shirley, Local screening of a core hole: A real-space approach applied to hafnium oxide, *Ultramicroscopy* **106**, 986 (2006).

² N. Wiser, Dielectric constant with local field effects included, *Phys. Rev.* **129**, 62 (1963).

³ H. N. Rojas, R. W. Godby, and R. J. Needs, Space-time method for ab initio calculations of self-

energies and dielectric response functions of solids, *Phys. Rev. Lett.* **74**, 1827 (1995).

⁴ X. Blase, A. Rubio, S. G. Louie, and M. L. Cohen, Mixed-space formalism for the dielectric response in periodic systems, *Phys. Rev. B* **52**, R2225 (1995).

⁵ L. Hung, F. H. da Jornada, J. Souto-Casares, J. R. Chelikowsky, S. G. Louie, and S. Ögüt, Excitation spectra of aromatic molecules within a real-space gw -bse for-

- malism: Role of self-consistency and vertex corrections, *Phys. Rev. B* **94**, 085125 (2016).
- ⁶ F. Giustino, M. L. Cohen, and S. G. Louie, *gw* method with the self-consistent sternheimer equation, *Phys. Rev. B* **81**, 115105 (2010).
- ⁷ H.-V. Nguyen, T. A. Pham, D. Rocca, and G. Galli, Improving accuracy and efficiency of calculations of photoemission spectra within the many-body perturbation theory, *Phys. Rev. B* **85**, 081101 (2012).
- ⁸ M. D. Ben, F. H. da Jornada, A. Canning, N. Wichmann, K. Raman, R. Sasanka, C. Yang, S. G. Louie, and J. Deslippe, Large-scale *gw* calculations on pre-exascale hpc systems, *Computer Physics Communications* **235**, 187 (2019).
- ⁹ M. M. Rieger, L. Steinbeck, I. White, H. Rojas, and R. Godby, The *gw* space-time method for the self-energy of large systems, *Computer Physics Communications* **117**, 211 (1999).
- ¹⁰ M. Kaltak, J. c. v. Klimeš, and G. Kresse, Cubic scaling algorithm for the random phase approximation: Self-interstitials and vacancies in si, *Phys. Rev. B* **90**, 054115 (2014).
- ¹¹ M. Kim, G. J. Martyna, and S. Ismail-Beigi, Complex-time shredded propagator method for large-scale *gw* calculations, *Phys. Rev. B* **101**, 035139 (2020).
- ¹² G. Onida, L. Reining, and A. Rubio, Electronic excitations: density-functional versus many-body green's-function approaches, *Rev. Mod. Phys.* **74**, 601 (2002).
- ¹³ Z. H. Levine and S. G. Louie, New model dielectric function and exchange-correlation potential for semiconductors and insulators, *Phys. Rev. B* **25**, 6310 (1982).
- ¹⁴ E. L. Shirley, J. A. Soininen, and J. J. Rehr, Modeling core-hole screening in core-excitation spectroscopies, *Physica Scripta* **T115**, 31 (2005).
- ¹⁵ J. Vinson, J. J. Rehr, J. J. Kas, and E. L. Shirley, Bethe-salpeter equation calculations of core excitation spectra, *Phys. Rev. B* **83**, 115106 (2011).
- ¹⁶ K. Gilmore, J. Vinson, E. Shirley, D. Prendergast, C. Pemasaraju, J. Kas, F. Vila, and J. Rehr, Efficient implementation of core-excitation bethe-salpeter equation calculations, *Comput. Phys. Comm.* **197**, 109 (2015).
- ¹⁷ R. M. Martin, *Electronic Structure: Basic Theory and Practical Methods* (Cambridge University Press, Cambridge, United Kingdom, 2004).
- ¹⁸ L. Kleinman and D. M. Bylander, Efficacious form for model pseudopotentials, *Phys. Rev. Lett.* **48**, 1425 (1982).
- ¹⁹ E. L. Shirley, Bethesalpeter treatment of x-ray absorption including core-hole multiplet effects, *Journal of Electron Spectroscopy and Related Phenomena* proceeding of the Fourteenth International Conference on Vacuum Ultraviolet Radiation Physics. **144-147**, H187, (2005).
- ²⁰ P. E. Blöchl, Projector augmented-wave method, *Phys. Rev. B* **50**, 17953 (1994).
- ²¹ J. J. Sakurai, *Modern Quantum Mechanics*, edited by S. F. Tuan (Addison-Wesley Publishing Company, Inc., Reading, MA, 1994).
- ²² K. Pearson, On lines and planes of closest fit to systems of points in space, *The London, Edinburgh, and Dublin Philosophical Magazine and Journal of Science* **27**, 69 (1901).
- ²³ I. S. Dhillon and B. N. Parlett, Multiple representations to compute orthogonal eigenvectors of symmetric tridiagonal matrices, *Linear Algebra and its Applications* **387**, 1 (2004).
- ²⁴ E. Anderson, Z. Bai, C. Bischof, S. Blackford, J. Demmel, J. Dongarra, J. Du Croz, A. Greenbaum, S. Hammarling, A. McKenney, and D. Sorensen, *LAPACK Users' Guide*, 3rd ed. (Society for Industrial and Applied Mathematics, Philadelphia, PA, 1999).
- ²⁵ P. Giannozzi, O. Andreussi, T. Brumme, O. Bunau, M. B. Nardelli, M. Calandra, R. Car, C. Cavazzoni, D. Ceresoli, M. Cococcioni, N. Colonna, I. Carnimeo, A. D. Corso, S. de Gironcoli, P. Delugas, R. A. DiStasio, A. Ferretti, A. Floris, G. Fratesi, G. Fugallo, R. Gebauer, U. Gerstmann, F. Giustino, T. Gorni, J. Jia, M. Kawamura, H.-Y. Ko, A. Kokalj, E. Kçkbenli, M. Lazzeri, M. Marsili, N. Marzari, F. Mauri, N. L. Nguyen, H.-V. Nguyen, A. O. de-la Roza, L. Paulatto, S. Poncè, D. Rocca, R. Sabatini, B. Santra, M. Schlipf, A. P. Seitsonen, A. Smogunov, I. Timrov, T. Thonhauser, P. Umari, N. Vast, X. Wu, and S. Baroni, Advanced capabilities for materials modelling with quantum ESPRESSO, *Journal of Physics: Condensed Matter* **29**, 465901 (2017).
- ²⁶ P. Giannozzi, S. Baroni, N. Bonini, M. Calandra, R. Car, C. Cavazzoni, D. Ceresoli, G. L. Chiarotti, M. Cococcioni, I. Dabo, *et al.*, Quantum espresso: a modular and open-source software project for quantum simulations of materials, *J. Phys. Condens. Matter* **21**, 395502 (2009); www.quantum-espresso.org.
- ²⁷ J. P. Perdew and Y. Wang, Accurate and simple analytic representation of the electron-gas correlation energy, *Phys. Rev. B* **45**, 13244 (1992).
- ²⁸ M. van Setten, M. Giantomassi, E. Bousquet, M. Verstraete, D. Hamann, X. Gonze, and G.-M. Rignanese, The pseudodojo: Training and grading a 85 element optimized norm-conserving pseudopotential table, *Computer Physics Communications* **226**, 39 (2018); <http://www.pseudo-dojo.org> Scalar-relativistic v. 0.4.
- ²⁹ D. R. Hamann, Optimized norm-conserving vanderbilt pseudopotentials, *Phys. Rev. B* **88**, 085117 (2013); The open-source code ONCVSP is available at <http://www.mat-simresearch.com> v. 3.3.1.
- ³⁰ C. P. Schwartz, F. Ponce, S. Friedrich, S. P. Cramer, J. Vinson, and D. Prendergast, Temperature and radiation effects at the fluorine k-edge in lif, *Journal of Electron Spectroscopy and Related Phenomena* **218**, 30 (2018).
- ³¹ T. A. Pascal, U. Boesenberg, R. Kostecki, T. J. Richardson, T.-C. Weng, D. Sokaras, D. Nordlund, E. McDermott, A. Moewes, J. Cabana, and D. Prendergast, Finite temperature effects on the x-ray absorption spectra of lithium compounds: First-principles interpretation of x-ray raman measurements, *The Journal of Chemical Physics* **140**, 034107 (2014).
- ³² ~~144-147, H187, (2005)~~ method for calculating the one-particle green's function with application to the electron-gas problem, *Phys. Rev.* **139**, A796 (1965).
- ³³ C. Vorwerk, C. Cocchi, and C. Draxl, Addressing electron-hole correlation in core excitations of solids: An all-electron many-body approach from first principles, *Phys. Rev. B* **95**, 155121 (2017).
- ³⁴ W. Gao and J. R. Chelikowsky, Real-space based benchmark of g0w0 calculations on gw100: Effects of semicore orbitals and orbital reordering, *Journal of Chemical Theory and Computation* **15**, 5299 (2019).
- ³⁵ B.-C. Shih, Y. Xue, P. Zhang, M. L. Cohen, and S. G. Louie, Quasiparticle band gap of zno: High accuracy from the conventional G^0W^0 approach, *Phys. Rev. Lett.* **105**, 146401 (2010).

- ³⁶ L. X. Benedict and E. L. Shirley, Ab initio calculation of $\epsilon_2(\omega)$ including the electron-hole interaction: Application to gan and caf₂, *Phys. Rev. B* **59**, 5441 (1999).
- ³⁷ H. M. Lawler, J. J. Rehr, F. Vila, S. D. Dalosto, E. L. Shirley, and Z. H. Levine, Optical to uv spectra and birefringence of sio₂ and tio₂: First-principles calculations with excitonic effects, *Phys. Rev. B* **78**, 205108 (2008).
- ³⁸ M. S. Hybertsen and S. G. Louie, Ab initio static dielectric matrices from the density-functional approach. i. formulation and application to semiconductors and insulators, *Phys. Rev. B* **35**, 5585 (1987).
- ³⁹ W. Hanke and L. J. Sham, Many-particle effects in the optical excitations of a semiconductor, *Phys. Rev. Lett.* **43**, 387 (1979).
- ⁴⁰ R. W. G. Wyckoff, *Crystal Structures*, 2nd ed. (Interscience Publishers, New York, 1963).
- ⁴¹ C. Kittel, *Introduction to Solid State Physics*, 8th ed. (John Wiley & Sons, Inc, 2005).
- ⁴² P. Puschnig and C. Ambrosch-Draxl, Optical absorption spectra of semiconductors and insulators including electron-hole correlations: An ab initio study within the lapw method, *Phys. Rev. B* **66**, 165105 (2002).
- ⁴³ M. Gatti and F. Sottile, Exciton dispersion from first principles, *Phys. Rev. B* **88**, 155113 (2013).
- ⁴⁴ M. Piacentini, D. W. Lynch, and C. G. Olson, Thermoreflectance of lif between 12 and 30 ev, *Phys. Rev. B* **13**, 5530 (1976).
- ⁴⁵ X. Zhu and S. G. Louie, Quasiparticle band structure of thirteen semiconductors and insulators, *Phys. Rev. B* **43**, 14142 (1991).
- ⁴⁶ A form of this has been attributed to Enrico Fermi.
- ⁴⁷ M. Frigo and S. G. Johnson, The design and implementation of FFTW3, *Proceedings of the IEEE* **93**, 216 (2005), special issue on “Program Generation, Optimization, and Platform Adaptation”.
- ⁴⁸ A. Ware, Fast approximate fourier transforms for irregularly spaced data, *SIAM Review* **40**, 838 (1998).
- ⁴⁹ Specific hardware is named for identification purposes; it does not imply recommendation or endorsement by NIST. The CPUs used were Intel Xeon E5-2630 v3.
- ⁵⁰ I. H. Sloan and R. S. Womersley, Extremal systems of points and numerical integration on the sphere, *Advances in Computational Mathematics* **21**, 107 (2004).
- ⁵¹ C. Friedrich, M. C. Müller, and S. Blügel, Band convergence and linearization error correction of all-electron *GW* calculations: The extreme case of zinc oxide, *Phys. Rev. B* **83**, 081101 (2011).
- ⁵² J. Vinson, T. Jach, W. T. Elam, and J. D. Denlinger, Origins of extreme broadening mechanisms in near-edge x-ray spectra of nitrogen compounds, *Phys. Rev. B* **90**, 205207 (2014).
- ⁵³ M. Rieder, J. C. Crelling, O. ustai, M. Drbek, Z. Weiss, and M. Klementov, Arsenic in iron disulfides in a brown coal from the north bohemian basin, czech republic, *International Journal of Coal Geology* **71**, 115 (2007).
- ⁵⁴ R. Del Sole, L. Reining, and R. W. Godby, *gw* Γ approximation for electron self-energies in semiconductors and insulators, *Phys. Rev. B* **49**, 8024 (1994).
- ⁵⁵ A. J. Morris, M. Stankovski, K. T. Delaney, P. Rinke, P. García-González, and R. W. Godby, Vertex corrections in localized and extended systems, *Phys. Rev. B* **76**, 155106 (2007).
- ⁵⁶ F. Bruneval, F. Sottile, V. Olevano, R. Del Sole, and L. Reining, Many-body perturbation theory using the density-functional concept: Beyond the *gw* approximation, *Phys. Rev. Lett.* **94**, 186402 (2005).
- ⁵⁷ M. L. Tiago and J. R. Chelikowsky, Optical excitations in organic molecules, clusters, and defects studied by first-principles green’s function methods, *Phys. Rev. B* **73**, 205334 (2006).
- ⁵⁸ J. P. Perdew and A. Zunger, Self-interaction correction to density-functional approximations for many-electron systems, *Phys. Rev. B* **23**, 5048 (1981).
- ⁵⁹ S. H. Vosko, L. Wilk, and M. Nusair, Accurate spin-dependent electron liquid correlation energies for local spin density calculations: a critical analysis, *Canadian Journal of Physics* **58**, 1200 (1980).
- ⁶⁰ D. M. Ceperley and B. J. Alder, Ground state of the electron gas by a stochastic method, *Phys. Rev. Lett.* **45**, 566 (1980).
- ⁶¹ F. Bruneval and X. Gonze, Accurate *gw* self-energies in a plane-wave basis using only a few empty states: Towards large systems, *Phys. Rev. B* **78**, 085125 (2008).
- ⁶² J. A. Berger, L. Reining, and F. Sottile, Ab initio calculations of electronic excitations: Collapsing spectral sums, *Phys. Rev. B* **82**, 041103 (2010).
- ⁶³ J. A. Berger, L. Reining, and F. Sottile, Efficient *gw* calculations for sno₂, zno, and rubrene: The effective-energy technique, *Phys. Rev. B* **85**, 085126 (2012).
- ⁶⁴ R. James and S. Woodley, Extraction of green’s functions from total energy plane wave pseudopotential calculations, *Solid State Communications* **97**, 935 (1996).
- ⁶⁵ L. Steinbeck, A. Rubio, L. Reining, M. Torrent, I. White, and R. Godby, Enhancements to the gw space-time method, *Computer Physics Communications* **125**, 105 (2000).
- ⁶⁶ G. Samsonidze, M. Jain, J. Deslippe, M. L. Cohen, and S. G. Louie, Simple approximate physical orbitals for *gw* quasiparticle calculations, *Phys. Rev. Lett.* **107**, 186404 (2011).
- ⁶⁷ H. Lambert and F. Giustino, Ab initio sternheimer-gw method for quasiparticle calculations using plane waves, *Phys. Rev. B* **88**, 075117 (2013).
- ⁶⁸ H. F. Wilson, F. m. c. Gygi, and G. Galli, Efficient iterative method for calculations of dielectric matrices, *Phys. Rev. B* **78**, 113303 (2008).
- ⁶⁹ D. Golze, J. Wilhelm, M. J. van Setten, and P. Rinke, Core-level binding energies from gw: An efficient full-frequency approach within a localized basis, *Journal of Chemical Theory and Computation* **14**, 4856 (2018).
- ⁷⁰ S. Baroni, S. de Gironcoli, A. Dal Corso, and P. Giannozzi, Phonons and related crystal properties from density-functional perturbation theory, *Rev. Mod. Phys.* **73**, 515 (2001).
- ⁷¹ X. Gonze, First-principles responses of solids to atomic displacements and homogeneous electric fields: Implementation of a conjugate-gradient algorithm, *Phys. Rev. B* **55**, 10337 (1997).
- ⁷² X. Gonze and C. Lee, Dynamical matrices, born effective charges, dielectric permittivity tensors, and interatomic force constants from density-functional perturbation theory, *Phys. Rev. B* **55**, 10355 (1997).
- ⁷³ A. A. Quong and B. M. Klein, Self-consistent-screening calculation of interatomic force constants and phonon dispersion curves from first principles, *Phys. Rev. B* **46**, 10734 (1992).